

Star Formation in Two Luminous Spiral Galaxies

Deidre A. Hunter¹, Bruce G. Elmegreen², Vera C. Rubin³, Allison Ashburn^{1,4}, Teresa Wright^{1,5}, Gyula I. G. Józsa^{6,7}, and Christian Struve⁶

ABSTRACT

We have examined star formation in two very luminous ($M_V = -22$ to -23) Sc-type spiral galaxies, NGC 801 and UGC 2885, using ultra-deep $H\alpha$ images. We combine these with UBV and 2MASS JHK images and HI maps to explore the star formation characteristics of disk galaxies at high luminosity. $H\alpha$ traces star formation in these galaxies to 4-6 disk scale lengths, but the lack of detection of $H\alpha$ further out is likely due to loss of Lyman continuum photons. Considering gravitational instabilities alone, we find that the gas and stars in the outer regions are marginally stable in an average sense, but considering dissipative gas and radial and azimuthal forcing, the outer regions are marginally unstable to form spiral arms. Star formation is taking place in spiral arms, which are regions of locally higher gas densities. Furthermore, we have traced smooth exponential stellar disks over 3-orders of magnitude and 4-6 disk scale lengths, in spite of a highly variable gravitational instability parameter. Thus, gravitational instability thresholds do not seem relevant to the stellar disk. One possibility for creating an exponential disk is that the molecular cloud densities and star formation rates have exponential profiles and this forces the stellar disk to build up such a profile. Another possibility is that the stellar disk is continuously adjusted to an exponential shape regardless of the star formation profile, for example through global dynamical process that scatter stars. However, such scattering processes

¹Lowell Observatory, 1400 West Mars Hill Road, Flagstaff, Arizona 86001 USA

²IBM T. J. Watson Research Center, PO Box 218, Yorktown Heights, New York 10598 USA

³Carnegie Institution of Washington, 5241 Broad Branch Road NW, Washington, DC 20015

⁴Current address: Benedictine College, 1020 North 2nd St., Atchison, KS 66002 USA

⁵Current address: Department of Astronomy, Indiana University, 727 East 3rd St., Bloomington, IN 47405-7105 USA

⁶ASTRON (Netherlands Organisation for Scientific Research NWO), Oude Hoogeveensedijk 4, 7991 PD Dwingeloo, The Netherlands

⁷Argelander-Institut für Astronomie, Auf dem Hügel 71, D-53121 Bonn, Germany

are only known to operate in spiral systems, in which case they cannot explain the same dilemma of smooth exponential disks observed in dwarf irregular galaxies.

Subject headings: galaxies: spiral — galaxies: star formation — galaxies: individual (NGC 801, UGC 2885)

1. Introduction

In the Milky Way we see that stars form from clouds of molecular H_2 , and there is a correlation between the locations of molecular clouds and newly minted young stars. Presumably the molecular clouds form from atomic gas, but what are the conditions for clouds to form in a particular region? Star formation in the inner regions of spiral galaxies is usually attributed to gravitational instabilities following Toomre’s (1964) condition for collapse (Quirk 1972; Kennicutt 1989). However, this condition does not explain star formation in the outer parts or in dwarf irregular (dIrr) galaxies where the gas appears to be more stable. Furthermore, empirical relationships between gas and star formation (Kennicutt et al. 2007; Bigiel et al. 2008) become less predictive in dwarfs and the outer parts of spirals where the range in star formation rates (SFRs) is large for a given total gas density (Bigiel et al. 2010; Barnes et al. 2012; Ficut-Vicas, in prep).

Yet, stellar disks are traced to extraordinarily large radii, well out into the accompanying gas disks (see, for example, Ferguson et al. 1998, Ferguson & Johnson 2001, Bland-Hawthorn et al. 2005, Carraro et al. 2010, Vlajić et al. 2011, Eufrazio et al. 2013), and young stars *are* found in these outer disks. Stars younger than <0.5 Gyr are traced to 8 disk scale lengths in NGC 2403 (Barker et al. 2012) and 10 inner disk scale lengths in M33 (Grossi et al. 2011). In NGC 7793 (Radburn-Smith et al. 2012), M33 (Grossi et al. 2011), M83 (Bigiel et al. 2010), CIG96 (Espada et al. 2011), several other spiral galaxies (Barnes et al. 2012) and several dIrr (Hunter et al. 2011), star formation continues in the outer parts down to an H I column density of a few $M_\odot \text{ pc}^{-2}$ or less. *GALEX* has revealed UV-bright stellar complexes in M83 to 7 kpc (Thilker et al. 2005). Even in dwarf galaxies, like the LMC, young stars ($<$ few Gyr old) are found to 8 disk scale lengths (Saha et al. 2010).

Here we discuss star formation in two of the most luminous and massive Sc-type galaxies in the nearby universe (Burstein et al. 1982). These galaxies, NGC 801 and UGC 2885, were originally observed as part of a study of the rotation curves of spirals by Rubin et al. (1980). We obtained extremely deep H α images of these galaxies in order to trace H II regions into the outer disk. These data were originally taken for the purpose of extending the optical rotation curves further out into the disk, but here we use them as tracers of star formation.

Characteristics of the galaxies are given in Table 1. We combine the $H\alpha$ data with *UBV* and Two Micron All Sky Survey (2MASS) *JHK* images to trace the stellar populations and HI maps that reveal the atomic gas. With these data we examine the star formation properties of the galaxies: How far out can we trace star-forming regions? How does the star formation activity compare with the density of gas? Are these very luminous galaxies different compared to less luminous spirals, and how do their outer disks compare with low luminosity dwarf galaxies? And, what do the data tell us about the disk assembly of luminous spirals?

2. Observations and Data

2.1. $H\alpha$ Imaging

Deep $H\alpha$ images were obtained 2007 November 6-12 using the T2KB 2048×2048 direct imaging CCD on the 2.1 m telescope at Kitt Peak National Observatory (KPNO¹). For the on-band filter, we used KPNO #1495, which has a passband center at 6691 Å and FWHM of 78 Å. We used filter #1564 for the off-band (stellar continuum). The off-band filter is centered at 6618 Å with a FWHM of 74 Å. The pixel scale was 0.304'' per pixel for a field of view of 10.4'. We used observations of the flat-field screen in the dome to correct for pixel-to-pixel variations. We also observed spectrophotometric standard stars at several airmasses to correct for extinction by the earth's atmosphere and to transform counts in the $H\alpha$ images to $\text{ergs s}^{-1} \text{cm}^{-2}$. The FWHM of stars on the $H\alpha$ images are 1.5'' for NGC 801 and 1.3'' for UGC 2885.

For the galaxies, the observing sequence was off-band, $H\alpha$, $H\alpha$, off-band, $H\alpha$, $H\alpha$, off-band, and so forth. Each exposure was 1800 s. There were 24 $H\alpha$ images of NGC 801 and 28 of UGC 2885 for a total on-band exposure time of 12 and 14 hours, respectively. All images were shifted and scaled to match one of the $H\alpha$ images for each galaxy. The off-band images were also shifted and scaled to the on-band image in order to subtract the stellar continuum. The final $H\alpha$ image of NGC 801 has a stellar FWHM of 1.4'', and that of UGC 2885 has 1.3''. The $H\alpha$ image was geometrically transformed to match the scale and orientation of the *V*-band image so that we could use the same parameters for surface photometry as was used for the broad-band imaging.

¹Kitt Peak National Observatory, National Optical Astronomy Observatory, which is operated by the Association of Universities for Research in Astronomy (AURA) under cooperative agreement with the National Science Foundation.

The rms in the sky-subtracted, edited H α images is $3\text{-}4 \times 10^{-18}$ ergs s $^{-1}$ cm $^{-2}$. Thus, the rms includes the sky-subtraction and residuals due to editing foreground stars. This rms translates to about 3×10^{36} ergs s $^{-1}$ per pixel at the distance of these galaxies. The FWHM of stars in the H α images is about 2 pixels, and the area covered is about 3 pixels. Thus, an unresolved H II region at a level of one rms would have a luminosity of about 9×10^{36} ergs s $^{-1}$, approximately one Orion nebula (Kennicutt 1984).

2.2. *UBV* Imaging

UBV images of NGC 801 and UGC 2885 were obtained 2010 December 1 and 27-28 with an e2v 2048 \times 2048 CCD on the Lowell 1.1 m Hall telescope. The CCD was binned 2 \times 2 for a pixel scale of 0.74". Exposure times were 600 s in *V*, 1200 s in *B*, and 1800 s in *U*. We obtained 10/6/4 exposures in *V/B/U* of NGC 801 for total exposure times of 1.7/2.0/2.0 hrs, respectively. For UGC 2885 we have 10/7/6 exposures in *V/B/U* for total exposure times of 1.7/2.3/3.0 hrs, respectively. We used observations of the twilight sky to remove pixel-to-pixel variations across the CCD. We also observed Landolt (1992) standard stars for photometric calibrations. The rms in the *U*-band calibration is 0.042 mag, for *B* it is 0.036 mag, and for *V* it is 0.028 mag. Stars on the final *V*-band image of NGC 801 have a FWHM of 1.9" and on the UGC 2885 image have a FWHM of 2.4".

All of the images in a given filter were aligned, scaled, and averaged to produce a single final image. The *B*-band image was also shifted to match the *V*-band image and the *U*-band was geometrically transformed to match *V*. Foreground stars and background objects were edited from the images and the non-galaxy portion of the CCD images were fit to determine the two-dimensional background using IMSURFIT in the *Image Reduction and Analysis Facility* (IRAF²). The background was subtracted from the image to produce a sky-subtracted image ready for surface photometry. The center of the galaxy, the position angle (PA) of its major axis, and its minor-to-major axis ratio *b/a* were measured from an outer isophote in the *V*-band image. The center of the galaxy was determined from a radial profile of the nucleus/bulge.

²IRAF is distributed by the National Optical Astronomy Observatory, which is operated by the Association of Universities for Research in Astronomy (AURA) under cooperative agreement with the National Science Foundation.

2.3. *JHK* Imaging

We obtained *JHK* images of the galaxies from the 2MASS online archives of the All-Sky Release Survey Atlas. Before performing surface photometry, we geometrically transformed them to match the scale and orientation of the *V*-band image, and, as for the other images, edited non-galaxy objects from the image, fit the 2D background, and subtracted it from the images. The FWHM of stars in the frames were 2.4''-2.5'' on the NGC 801 images and 2.7''-2.8'' on the UGC 2885 images. The 2MASS images come with calibration information in their headers. These images are not very deep, but they give us the *JHK* colors of the central regions of the galaxies.

We also examined the *Spitzer* 3.6 μm images of these galaxies, but the field of view was too small to allow adequate sky-subtraction. Hence, the photometry was unreliable.

2.4. H I-line Data

H I-line data were available for both galaxies from the archives of the Westerbork Synthesis Radio Telescope (WSRT). NGC 801 was observed as part of the Westerbork Observations of Neutral Hydrogen in Irregular and Spiral Galaxies (WHISP, see van der Hulst et al. 2001) project and the data were provided to us. The beam size is 16.1'' \times 27.0'', and the channel separation and spectral resolution is 8.25 km s⁻¹. The map cubes are 512 \times 512 pixels and each pixel is 5.0''. The rms noise in a channel map of the data cube is 0.73 mJy beam⁻¹. From the data cube we determine a total flux of 20.96 Jy km s⁻¹, corresponding to an H I mass of $3.0 \times 10^{10} M_{\odot}$. This is similar to the H I mass of $2.6 \times 10^{10} M_{\odot}$, corrected for distance, given by the WHISP project (<http://www.astro.rug.nl/~whisp/>).

UGC 2885 was observed with the WSRT in 2004 in two runs with a total on-source integration time of 24 h. The total bandwidth was 10 MHz with a number of 1024 channels, centered on the H I line of UGC 2885. We used two parallel-handed polarization products without online Hanning smoothing. The data underwent a standard data reduction with the Miriad software package (Sault et al. 1995). The data were flagged, and a primary bandpass calibration was applied. After that, an iterative self-calibration on the continuum image was performed to correct the frequency-independent gains. The data were Hanning-smoothed, continuum-subtracted, gridded and inverted using a set of different weighting schemes, and subsequently deconvolved employing the CLEAN algorithm. For the latter we used an iterative approach in which we successively decreased the cutoff level and increased “clean regions,” restricting CLEAN to certain areas in the single planes of the cubes. For this study, a data cube employing a Robust weighting of 0.0 without averaging in frequency

was found to be most suitable. The resulting spatial resolution is $22.3'' \times 13.6''$ (HPBW), the channel width is 2.06 km s^{-1} , and the rms noise is $0.63 \text{ mJy beam}^{-1}$. The adopted data cube has a size of 256×256 pixels and a pixel size of $4''$. From this data cube, we determined the total HI flux of UGC 2885 to be $28.3 \text{ Jy km s}^{-1}$, which corresponds to an HI mass of $4.2 \times 10^{10} M_{\odot}$.

Note that there is another galaxy in the field of view of the NGC 801 map. The galaxy, NGC 797, to the southwest of NGC 801 has a recessional velocity that is 110 km s^{-1} smaller than NGC 801's and the two galaxies are 215 kpc apart on the sky at a distance of 79.4 Mpc. NGC 797 is classed as an SAB(s)a by de Vaucouleurs et al. (1991). The integrated HI map showing both galaxies is displayed in Figure 1. From here on, only the region immediately around NGC 801 will be shown.

3. Analysis

3.1. Surface Photometry

The V -band, $\text{H}\alpha$, and integrated HI images of NGC 801 and UGC 2885 are shown in Figures 2 and 3. Both galaxies are seen fairly edge-on; inclinations are 74° and 82° .

We performed azimuthally-averaged surface photometry on the $UBVJHK$ and $\text{H}\alpha$ images using ELLIPSE in IRAF. We began with the edited, sky-subtracted images, all geometrically transformed to match the scale and orientation of the V -band image, and used the parameters derived from the V -band image to define the ellipse shape and orientation (see Table 1). We held the center, PA of the major axis, and ellipticity of successive ellipses constant and used a step size of $14.8''$ for the semi-major axis. Annular surface photometry was determined by subtracting two adjacent ellipses and dividing by the area in the annulus.

Although we edited the images of foreground and background objects, there were some artifacts from nearby bright stars or fainter stars within the galaxy image that were masked. UGC 2885, in particular, has a bright star to the northeast of the galaxy center, so much of that half of the galaxy had to be masked. Masked regions were replaced with average photometry in the annulus. The azimuthally-averaged surface photometry, not corrected for reddening, is shown in Figures 5 and 6.

Similar to the stellar photometry, we determined the HI surface densities from the integrated HI maps using the Groningen Image Processing System (GIPSY, Vogelaar & Terlouw 2001). The ellipse parameters and step size were the same as those for the optical and near-IR images.

3.2. Extinction and Reddening

Correcting the surface photometry for extinction due to dust includes foreground reddening due to the Milky Way $E(B-V)_f$ and reddening internal to the galaxy $E(B-V)_i$. The total reddening $E(B-V)_t$ is the sum of these two components. For $E(B-V)_f$ we use the values given in the NASA/IPAC Extragalactic Database (NED) for the recalibration of the Schlegel et al. (1998) values by Schlafly & Finkbeiner (2011). The $E(B-V)_f$ are given in Table 1. To correct for the foreground extinction we use the Cardelli et al. (1989) extinction law that was determined for the Milky Way: $A_{V,f} = 3.1 \times E(B-V)_f$, $E(U-B)_f = 0.69 \times E(B-V)_f$, $E(J-H)_f = 0.27 \times E(B-V)_f$, $E(H-K)_f = 0.23 \times E(B-V)_f$, and $E(V-J)_f = 2.14 \times E(B-V)_f$.

We have no direct measurement of $E(B-V)_i$ for our galaxies, and so we estimate them from observations of other galaxies in the literature. One complication is that extinction may be a function of galaxy luminosity (Wang & Heckman 1996) and in spirals it changes with radius, decreasing into the outer disk (Huizinga & van Albada 1992). We began with the work of Prescott et al. (2007), a study of star-forming regions in galaxies observed as part of the *Spitzer* Infrared Nearby Galaxies Survey (SINGS). Fitting their Figure 12, we have that the internal V -band extinction of star-forming nebulae is $\log A_{V,i}^{\text{HII}} = 0.45 - 0.67 \times (R/R_{25})$. Their data only extend to an R/R_{25} of 1.4, so we extrapolate this to R/R_{25} of 3 for our data. The values from Prescott et al. (2007) were determined for star-forming regions, and are appropriate for our $H\alpha$ photometry of H II regions. We adopt $A_{H\alpha,i}^{\text{HII}} = 0.82 A_{V,i}^{\text{HII}}$, which Prescott et al. took from Calzetti et al. (2000).

We expect field stars to suffer from less extinction than star-forming regions in dense clouds, and so for the field stars we turn to the extinction law of Calzetti et al. (1994, 2000). This extinction law was determined specifically for the stellar continuum integrated over large regions in starburst galaxies. Our spirals are not strictly speaking “starburst” systems, but they are actively forming stars. For scaling the extinction law, $E(B-V)_i^*$, we use the observation that the reddening of the stars is related to that of the ionized gas in star-forming regions, on average, as $E(B-V)_i^* = 0.44 \pm 0.03 E(B-V)_i^{\text{HII}}$ (Calzetti 1997). Thus, we use the $A_{V,i}^{\text{HII}}$ determined from Prescott et al. (2007) for the ionized gas, divide that by $R_V = 4.05$ (Calzetti et al. 2000) to obtain $E(B-V)_i^{\text{HII}}$, and multiply that by 0.44 to obtain $E(B-V)_i^*$. The Calzetti et al. extinction law can then be used to correct the photometry of the stellar populations in the various broad-band filters: $A_{V,i}^* = 4.05 \times E(B-V)_i^*$, $E(U-B)_i^* = 0.95 \times E(B-V)_i^*$, $E(J-H)_i^* = 0.57 \times E(B-V)_i^*$, $E(H-K)_i^* = 0.43 \times E(B-V)_i^*$, and $E(V-J)_i^* = 0.97 \times E(B-V)_i^*$. $E(B-V)_i^{\text{HII}}$ and $E(B-V)_i^*$ are shown as a function of radius in Figure 4. From this we have that $E(B-V)_i^{\text{HII}}$ is ~ 0.7 mag in the centers of the galaxies and drops to 0.01 at $R/R_{25} = 3$.

For integrated photometry, we use the $E(B-V)_i^*$ and $E(B-V)_i^{\text{HII}}$ appropriate to the

V -band half-light radius $R_{1/2}$ of the galaxy. $R_{1/2}$ was determined before any reddening correction was applied. Those values are given in Table 1.

Figure 7 shows the integrated UBV and JHK colors of NGC 801 and UGC 2885 on color-color diagrams. We also show $(U - B)_0$ and $(B - V)_0$ averages by spiral morphological type from de Vaucouleurs & de Vaucouleurs (1972), and the uncertainties are the spread in colors for each type. The arrow shows the reddening vector for $E(B-V)=0.1$. NGC 801 and UGC 2885 are redder than other Sc-type galaxies, comparable instead to Sb-type galaxies. For $(H - K)_0$ vs $(J - H)_0$, we show the average for spiral disks from Holwerda et al. (2005) and the uncertainties are the range of values in the average colors. The arrow is the reddening vector for $E(J-H)=0.1$. NGC 801 and UGC 2885 are redder than most other spirals in these colors too, but within the range of values seen.

The azimuthally-averaged surface photometry, corrected for reddening, are shown in Figures 8 and 9. In the top panel, $\log \Sigma_{H\alpha}$ and μ_V are plotted as a function of radius. The logarithmic interval is equal to the magnitude interval that is plotted, so that the shapes of the profiles of the two quantities $\log \Sigma_{H\alpha}$ and μ_V can be compared directly.

For NGC 801, the V -band surface photometry μ_V is high in the center, presumably due to the central bulge. Beyond 20 kpc, μ_V can be fit with a two-component exponential with an upbending outer part. The inner component fits $R = 20 - 40$ kpc and the outer $R = 40 - 60$ kpc, shown in Figure 8 as a dotted line and a solid line, respectively. The inner component is fit with a disk scale length R_D of 10.5 ± 0.4 kpc and a central surface brightness μ_V^0 of 22.0 ± 0.1 mag arcsec $^{-1}$. A fit to the outer disk yields a disk scale length R_D of 14.1 ± 0.5 kpc and a central surface brightness of 23.1 ± 0.1 mag arcsec $^{-1}$. The two components cross at a break radius of 39.4 kpc and a surface brightness of 26.1 mag arcsec $^{-1}$. Because we emphasize the outer disk here, we use the disk scale length of the outer surface brightness component.

We see that $\Sigma_{H\alpha}$ drops like μ_V with radius until a radius of 26 kpc, and then it declines faster. $H\alpha$ ends where the V surface photometry ends. The V -band image is not particularly deep, so it is possible that μ_V continues to lower surface brightness levels, but the $H\alpha$ exposure *is* deep and it is unlikely that $H\alpha$ would be detected much further out. In NGC 801 the $(B - V)_0$ and $(U - B)_0$ colors are red in the center and get slightly (~ 0.15 mag) bluer to a radius of about 25 kpc, approximately the same radius where the $H\alpha$ surface brightness begins to decline faster than μ_V . Beyond that radius $(B - V)_0$ stays constant within the uncertainties, and $(U - B)_0$ gets slightly (~ 0.16 mag) redder. There are only two annuli with JHK colors, but they are red and within the uncertainties constant over that limited radius range.

For UGC 2885, there is a small excess of μ_V in the inner 8.5 kpc, but beyond that we see an exponential disk. The disk scale length is 12.0 ± 0.4 kpc and μ_V^0 is 21.3 ± 0.1 mag in V . Here we see that $\Sigma_{H\alpha}$ is low in the center, and then from 8.5 kpc onward it declines with radius like μ_V . $H\alpha$ emission is traced to 74 kpc, similar to μ_V , which is traced to 71 kpc. The colors $(B - V)_0$ and $(U - B)_0$ are red in the center and get bluer ($\sim 0.25, 0.23$ mag) with radius to 31 kpc. Beyond that radius they stay approximately constant within the uncertainties, although the $(U - B)_0$ color exhibits a 0.1 mag offset to the red. There are only two annuli with JHK colors, but the colors are red in the center, and in $(H - K)_0$ and $(V - J)_0$ the colors are a bit redder in the second annulus compared to the first.

3.3. Determining Star Formation Rates

We use $H\alpha$ to determine the SFRs in NGC 801 and UGC 2885 using the formula of Kennicutt (1998). However, first we must correct the flux measured in the $H\alpha$ filter for the contribution by $[\text{NII}]\lambda 6548 + 6583$ emission. We must also correct the SFR formula for the metallicity of the stars since the output of ionizing photons changes with metallicity for a given stellar mass.

3.3.1. $[\text{NII}]$ Correction

The $H\alpha$ filter bandpass includes $[\text{NII}]\lambda 6548$ and $[\text{NII}]\lambda 6584$, and we need to subtract the contribution from $[\text{NII}]$ to the flux in order to derive pure $H\alpha$ emission. First, all three emission lines are located on the flat part of the transmission curve of the filter. That means that there is no difference in the transmission of the different emission lines, and we need only correct for the intrinsic relative fluxes of the emission lines. Second, from the $H\alpha$ survey of James et al. (2005), 5 spirals give a global average ratio $H\alpha / (H\alpha + [\text{NII}])$ of 0.82, where $[\text{NII}]$ is the sum of the emission from $\lambda 6548$ and $\lambda 6583$. So, we multiply our $H\alpha$ fluxes by 0.82 to correct for $[\text{NII}]$ emission.

3.3.2. Metallicity

Spiral galaxies typically exhibit abundance gradients with radius. For NGC 801 and UGC 2885 we adopt M81's oxygen abundance gradient as given by Patterson et al. (2012): -0.117 ± 0.073 dex R_{25}^{-1} . M81 has an integrated M_V of -20.8 , so it is less luminous than NGC 801 and UGC 2885 by a factor of 3-6. However, Henry & Worthey (1999) argue that

abundance gradients in spirals are independent of the absolute magnitude of the galaxy when the gradient is expressed in terms of radius normalized to R_{25} . We use Patterson’s “KK04” gradient, determined from 4 data sets, which has the advantage that the oxygen abundance $12 + \log(\text{O}/\text{H})$ at the center is 9.0. This is close to the maximum $12 + \log(\text{O}/\text{H})$ of 8.9 found by Pilyugin et al. (2007) at the centers of luminous ($M_B = -22.5$) spirals. Therefore, we adopted $12 + \log(\text{O}/\text{H}) = 9.0 - 0.12(R/R_{25})$ as the oxygen abundance as a function of radius in our spirals. This is shown in Figure 10. $12 + \log(\text{O}/\text{H})$ starts at 9.0 in the center and drops to 8.58, 78% solar, at $R/R_{25} = 3.5$. We use a solar oxygen abundance of 8.69 (Asplund et al. 2009).

3.3.3. The SFR Formula

To convert $\Sigma_{H\alpha}$ in units of $\text{ergs s}^{-1} \text{pc}^{-2}$, as shown in Figures 8 and 9, to SFR in units of $M_\odot \text{yr}^{-1} \text{kpc}^{-2}$, we begin with the formula of Kennicutt (1998): $\text{SFR}_{H\alpha} (M_\odot \text{yr}^{-1}) = 7.9 \times 10^{-42} L_{H\alpha} (\text{ergs s}^{-1})$. We multiply the $H\alpha$ surface density by 0.82 to remove [NII] and then adjust the formula for the deviation of the metallicity from solar, the abundance that Kennicutt used. For the latter, we use the synthesis models of STARBURST99 (Leitherer et al. 1999), with constant SFR and a Salpeter (1955) stellar initial mass function. Their Figure 78, which gives the number of photons below 912 Å, enables us to find the average flux of ionizing photons per second from a stellar population relative to that at solar and so to modify Kennicutt’s $H\alpha$ formula as a function of Z from twice solar to below solar. The correction factor at twice solar metallicity is 1.18 and at 40% solar is 0.87. We interpolate to determine the correction factor for the metallicity at a given radius. The derived SFRs for NGC 801 and UGC 2885 are shown in Figure 11.

Integrated SFRs use the oxygen abundance at the half-light radius to determine the SFR formula. For both galaxies this is approximately $z = 0.03$. Thus, the SFRs need to be multiplied by a factor of 1.089 to adjust for the metallicity. The integrated SFRs are given in Table 1.

We have also computed a SFR necessary to form the stellar mass that currently exists in each galaxy, SFR_V . For this we used the V -band surface brightness to determine the mass in stars and assume a timescale of 12 Gyr for the formation of that stellar mass. We obtain M/L_V as a function of $(B-V)_0$ from Bell & de Jong (2001). If the uncertainty in the color is greater than 0.1 mag, we use the average $(B-V)_0$ in the outer disk. SFR_V is the SFR necessary to produce the original mass in stars. Because the M/L_V yields the mass currently in stars, we correct this by a factor of two for the mass recycled back into the interstellar medium (Brinchmann et al. 2004) in order to use the total mass ever formed into stars in

computing the lifetime average SFR_V . The ratio $\text{SFR}_{H\alpha}/\text{SFR}_V$ is shown in Figure 12. We also compute the current surface density of the stellar mass Σ_* in units of $M_\odot \text{pc}^{-2}$.

4. Discussion

4.1. Extent of $H\alpha$ emission

The extent of $H\alpha$ emission in our two galaxies was determined by eye on the continuum-subtracted images. The furthest emission we detected in NGC 801 to the north of the galaxy has a surface brightness of $10 \times 10^{-18} \text{ ergs cm}^{-2} \text{ s}^{-1} \text{ arcsec}^{-2}$. In UGC 2885 the faintest region we traced to the southwest has an $H\alpha$ surface brightness of $5 \times 10^{-18} \text{ ergs cm}^{-2} \text{ s}^{-1} \text{ arcsec}^{-2}$. This represents the faintest surface brightness we could probably identify as a distinct region.

In NGC 801 the $H\alpha$ disk extends further to the northwest than to the southeast, and the furthest discrete H II region that we can identify is found at a radius of $\sim 55 \text{ kpc}$. The southeast H II regions only extend to 43 kpc . The local Σ_{HI} is $1 \times 10^{21} \text{ atoms cm}^{-2}$ at the radius of the most distant H II region. This HI column density is integrated along the line of sight for a highly inclined disk. Multiplying by the cosine of the inclination, 82° , to convert to the perpendicular surface density, we get $1.4 \times 10^{20} \text{ atoms cm}^{-2} = 1.5 M_\odot \text{pc}^{-2}$ including He and heavy elements. The outer H II regions in NGC 801 fall along the extensions of spiral arms. That star formation even in the outer disks of spirals is generally found associated with spiral arms seems to be a general feature of spiral galaxies (Ferguson et al. 1998, Thilker et al. 2007, Barnes et al. 2012). Outer star formation in dIrr galaxies, by contrast, is not in spiral arms, but in local clumps of high gas surface density (Hunter 1982, Hunter & Gallagher 1986).

On the northeast end of the disk of UGC 2885 there is an arc of H II regions, probably the end of a spiral arm, the tip of which is 68 kpc from the galactic center. The local Σ_{HI} there is $2 \times 10^{21} \text{ atoms cm}^{-2}$ which is $6.0 M_\odot \text{pc}^{-2}$ after correcting for inclination and heavy elements. On the southwest side of the galaxy, there are two possible faint detached H II regions at 60 kpc and 74 kpc . Off the major axis, there is a region to the southeast of center located at a de-projected radius of 74 kpc . These detached regions are located at Σ_{HI} of $8 \times 10^{20} \text{ atoms cm}^{-2}$ ($2.3 M_\odot \text{pc}^{-2}$ face-on).

In Figures 13 and 14 we show the azimuthally-averaged $H\alpha$ -based SFRs, $\Sigma_{\text{SFR},H\alpha}$, along with Σ_{HI} and the stellar mass surface density Σ_* . We see that the SFR drops 4 dex in NGC 801 from the center to a value of $10^{-6} M_\odot \text{yr}^{-1} \text{kpc}^{-2}$ at a radius of 60 kpc . In UGC 2885 it drops 1.5 dex to a value of $10^{-5} M_\odot \text{yr}^{-1} \text{kpc}^{-2}$ at 54 kpc . These very low SFRs in the outer

disks are comparable to those seen in less luminous Sab to Sd-type outer disks (Barnes et al. 2012) and in the outer disks (3-5 kpc radius) of dwarf galaxies (Hunter et al. 2011).

Some of the drop in H α at large radii could be from a loss of Lyman continuum photons from the vicinity of star formation (Beckman et al. 2000 [but see Lee et al. 2011], Hunter et al. 2010, Pellegrini et al. 2012). If we re-write the Strömgen relation as

$$nR_S = (3S/[4\pi R_S\alpha])^{1/2} \quad (1)$$

for ambient density n , Strömgen radius R_S , stellar ionization rate S , and case B recombination rate α , then the critical column density for trapping Lyman continuum radiation from an O-type star with $S = 10^{49} \text{ s}^{-1}$, considering $\alpha \sim 2.6 \times 10^{-13} \text{ cm}^3 \text{ s}^{-1}$ (Osterbrock 1989) and $R_S = 100R_2$ pc is

$$nR_{S,\text{crit}} = 1.7 \times 10^{20} R_2^{-1/2} \text{ cm}^{-2} = 1.9R_2^{-1/2} M_\odot \text{ pc}^{-2}. \quad (2)$$

To consider the possible loss of Lyman continuum photons from a region of star formation, the column density through a critical Strömgen diameter, $2nR_{S,\text{crit}}$, should be compared to the local average gas column density measured perpendicular in the disk. Equation (2) suggests that the critical value for trapping is $4 M_\odot \text{ pc}^{-2}$ or less for a single O-type star, especially if R_2 gets large in a disk flare. In fact, the most distant H II regions in our galaxies have local Σ_{HI} at about this limit or less. This suggests we could be missing other H II regions at these galactocentric distances and certainly missing those much further out. As a result, our estimates of star formation rates from outer disk H α should be considered lower limits.

The loss of ionizing radiation at extremely low Σ_{HI} is in addition to the loss studied by Relaño et al. (2012) that is for visible H II regions. They found that shell H II regions have lower H α compared to FUV than compact regions, indicating up to a 25% loss of ionization in the shell phase. If Σ_{HI} is as low as $\sim 2 M_\odot \text{ pc}^{-2}$, however, then even these visible H II regions should be difficult to see. First, there should be a loss of radiation from the disk because the Strömgen radius is larger than the scale height, which is the condition for the critical disk column density derived above.

Second, the emission from the fully ionized disk itself will be difficult to see because the emission measure is low. This fully ionized emission measure depends on the gas column density and scale height. The scale height is $\sigma^2/\pi G\Sigma_{\text{total}}$ for velocity dispersion σ and total mass column density in gas and stars, Σ_{total} . We assume $\sigma = 10 \text{ km s}^{-1}$ and take the total column densities from Figures 13 and 14. For NGC 801 at the outer annulus in the azimuthally-averaged surface photometry, $R \sim 60 \text{ kpc}$, $\Sigma_{\text{total}} = 0.6 M_\odot \text{ pc}^{-2}$, which gives a scale height of 13.1 kpc. For UGC 2885 at its outer annulus for H α detection, $R \sim 71 \text{ kpc}$, $\Sigma_{\text{total}} \sim 1.3 M_\odot \text{ pc}^{-2}$, and the scale height is 5.7 kpc.

The full disk thicknesses are twice these scale heights. If we take the measured $\Sigma_{\text{gas}} = 0.45 M_{\odot} \text{ pc}^{-2}$ at this radius in NGC 801 and correct for He and heavy elements, then the average H I density over the full thickness is 0.00052 cm^{-3} and the emission measure would be $0.0069 \text{ cm}^6 \text{ pc}$ if the disk is completely ionized. Similarly, for UGC 2885, where $\Sigma_{\text{gas}} = 1.18 M_{\odot} \text{ pc}^{-2}$, the density and emission measure would be 0.0031 cm^{-3} and $0.11 \text{ cm}^6 \text{ pc}$. Emission measure in H α converts to $\Sigma_{\text{H}\alpha}$ as shown in Figures 5, 6, 8, and 9 according to the equation

$$\Sigma_{\text{H}\alpha} (\text{erg s}^{-1} \text{ pc}^{-2}) = 7.7 \times 10^{30} EM (\text{cm}^6 \text{ pc}) \quad (3)$$

so the full-disk emission measures at the outer radii of the H II regions in these two galaxies convert to log-luminosity densities of $\log \Sigma_{\text{H}\alpha} = 28.7$ for NGC 801 and 29.9 for UGC 2885. In fact these are close to the minimum average luminosity densities for H α at the outer radii of these galaxies (Figures 8 and 9). We conclude again that we are probably missing H α emission and underestimating the H α SFR near the edges of these galaxies.

In NGC 801 we see that $\Sigma_{\text{SFR,H}\alpha}$ decreases with radius in the inner region like the surface density of the stellar mass even though the excess mass in the center is due to the galaxy bulge. Beyond a radius of 25 kpc, $\Sigma_{\text{SFR,H}\alpha}$ drops faster than Σ_{*} . This type of behavior is seen in other spirals as well (Christlein et al. 2010). However, beyond 25 kpc the H I gas surface density is about 4 times the stellar surface density and they both drop at nearly the same rate as far as our data trace the stars. Beyond our *V*-band image, the gas continues to decrease gently.

In the center of UGC 2885, there is a dip in the value of $\Sigma_{\text{SFR,H}\alpha}$. Beyond about 15 kpc radius, the azimuthally-averaged $\Sigma_{\text{SFR,H}\alpha}$ falls, more or less, like the surface density of the mass in stars, until 48 kpc. Beyond that radius $\Sigma_{\text{SFR,H}\alpha}$ drops more rapidly than Σ_{*} until both stars and H α emission are no longer detected at a radius of 71 kpc. At a radius of about 30 kpc, the H I and stellar mass surface densities are equal, and beyond that the stellar mass surface density drops more steeply than the gas, which continues to decrease gently, as in NGC 801. This lack of a correlation between outer disk star formation and outer disk gas is also evident in galaxies with large H I disks studied by Wang et al. (2013; in prep).

In NGC 801 and UGC 2885, we trace H α emission as far out as we trace *V*-band starlight. However, it is possible that young stars might be detectable in FUV emission even beyond where H α emission ends, since in outer disks UV light from young massive stars traces recent star formation more easily than H α emission from nebulae (as discussed above, and see, for example, Thilker et al. 2005, 2007; Boissier et al. 2007). Unfortunately, FUV images of these galaxies do not exist.

4.2. Radial trends in SFRs

In Figure 12 we show the ratio of current (≤ 10 Myr) SFR to the lifetime averaged SFR necessary to form the mass in stars, $\text{SFR}_{H\alpha}/\text{SFR}_V$, over 4-6 disk scale lengths. We find that the ratio is near 1 in the central regions of NGC 801, to a radius of $1.8R_D$. Beyond that in NGC 801 and everywhere in UGC 2885, the current SFR is significantly lower than the lifetime-averaged rate. For NGC 801 the ratio drops to 0.09 at a radius of $4R_D$. For UGC 2885 it is quite low (~ 0.01) in the center, rises to a high value of 0.6 at a radius of $2.6R_D$, and then drops slowly to a value of 0.07 at a radius of $6R_D$. Some of the drop in the perceived SFR in the far-outer regions could be from a loss of sensitivity to very faint H II regions there, considering that the H I column density is comparable to or lower than the critical value (Eq. 2) for trapping ionization in the nearby ambient medium.

In a deep imaging study of 5 dIrr galaxies we found a different situation (Hunter et al. 2011). In three of the dwarfs the ratio of current to lifetime-average SFR is roughly 1 at all radii. In the other two galaxies, the ratio is of order 0.1, so the current SFR is low compared to the past average. This low ratio is comparable to the maximum values in NGC 801 and UGC 2885. So, compared to dwarfs, these luminous spirals have formed much more of their stellar mass in the past than they are adding today.

The trends in NGC 801 and UGC 2885 are different from the general relationship seen in some spirals, as well. In a large sample of spirals, Ryder & Dopita (1994), found that the disk scale-length in H α is much longer than that of the V -band, and the V -band scale length is longer than that of the I -band surface photometry. Similarly, Chang et al. (2012) found in one gas-rich spiral that the recent SFR relative to the lifetime average increased as one moves to the outer disk. These types of observations are interpreted as evidence for an inside-out disk assembly model (e.g. Larson 1976; Chiappini et al. 1997; Mo et al. 1998; Naab & Ostriker 2006).

In UGC 2885 the inner part of the galaxy appears to be dominated by older stars while the outer disk is relatively younger, consistent in a general sense with inside-out growth. On the other hand, the current SFR drops relative to the lifetime average beyond a radius of $2.5R_D$. So, while the outer disk is younger than the central regions overall, the outer disk becomes more and more dominated by older stars with increasing radius. In NGC 801, however, the inner disk exhibits a constant SFR and then the current SFR drops steadily in the outer disk, beyond a radius of $2R_D$, compared to the lifetime average. This implies that the outer disk is relatively older than the inner disk, counter to inside-out disk growth models.

Yoachim et al. (2012) also find mixed star formation profiles in a sample of six nearby

spirals: half are dominated by an older stellar population beyond a break in the surface brightness profile, which they interpret as evidence for radial migration of older stars. Other studies have also found evidence for extended old stellar disks (see, for example, Ferguson & Johnson 2001, Vlajić et al. 2009). The other half of the Yoachim et al. sample shows no significant change in the stellar population in the outer disk. Thus, there does not seem to be a universal star formation profile among spirals (see also, Roediger et al. 2012).

The decrease in the ratio of current to past star formation in the outer regions of our galaxies, particularly in NGC 801, contradicts our expectation from the lack of a $B - V$ color gradient, which is shown in Figures 8 and 9. We seem to require some radial migration of stars to make the color gradients flat (e.g., Roškar et al. 2008).

4.3. The Toomre model

Toomre (1964) calculated the dispersion relation of self-gravitating waves in a thin rotating stellar disk and found a minimum velocity dispersion in the radial direction for stability. This critical velocity dispersion has found popular use in star formation models when it is re-written as a critical column density for gas Σ_{crit} . If the gas column density is greater than Σ_{crit} , then the model suggests star formation is active because of widespread instabilities. To check this model, we calculated Σ_{crit} as a function of radius for our galaxies using the rotation curves in Rubin et al. (1980). Σ_{crit} depends on the rotation curve through the epicyclic frequency κ : $\Sigma_{\text{crit}} = \kappa \sigma_g / \pi G$ for gas velocity dispersion σ_g . We assume $\sigma_g = 10 \text{ km s}^{-1}$, a typical spiral galaxy gaseous velocity dispersion (Tamburro et al. 2009). We also assume that the velocity dispersion is independent of radius, although there is evidence that the velocity dispersion is lower in outer spiral disks (Kamphuis & Sancisi 1993, Tamburro et al. 2009). The affect of lowering the velocity dispersion would be to decrease Σ_{crit} , making the gas proportionally more unstable against gravitational instabilities. The ratios of the observed Σ_{gas} to Σ_{crit} are shown for our two galaxies in Figure 15.

In the conventional instability model (e.g., Kennicutt 1989), stars should form at a greater rate where $\Sigma_{\text{gas}}/\Sigma_{\text{crit}}$ is higher. This is approximately true for our galaxies too. In both cases the ratio of the observed Σ_{gas} to Σ_{crit} is low in the center, climbs to a peak at mid-radius, and then drops in the outer disk. The radius at which $\Sigma_{\text{gas}}/\Sigma_{\text{crit}}$ begins to drop rapidly ($1.8\text{-}2.5R_D$) is also the same radius at which the current SFR drops relative to the integrated past SFR (Figure 12). However, this pattern is usually found in exponential disks with flat rotation curves, because then $\Sigma_{\text{gas}}/\Sigma_{\text{crit}} \propto R \exp(-R/R_D)$ for constant velocity dispersion regardless of star formation, and this function has the same general rising and falling shape as the observed profile. The low values of $\Sigma_{\text{gas}}/\Sigma_{\text{crit}}$ in the centers of our galaxies

could be from a high κ , a lack of gas, or the presence of molecules that are not included in Σ_{gas} . The maximum value of the ratio in NGC 801 is 0.7 and in UGC 2885 it is 0.6. At these peaks, the gas is close to the original Toomre (1964) critical density. However, at the maximum radius where H II regions are detected, the ratio is 0.2 in both NGC 801 and UGC 2885, which is far into the conventionally stable regime (see also the spirals in Barnes et al. 2012).

The low values of $\Sigma_{\text{gas}}/\Sigma_{\text{crit}}$ in the outer regions mean that stars are forming in gas that is sub-critical in the usual sense. This is similar to the situation in the outer disks of dIrr galaxies, even though the average H I column densities where the last H II regions are found in our spirals are higher than those in the outer disks of dwarfs by a factor of 10 (Hunter et al. 2011). Clearly, it is not H I column density alone that determines where stars form (but see Bigiel et al. 2010).

We also see no threshold or shift in the star formation rate at some characteristic $\Sigma_{\text{gas}}/\Sigma_{\text{crit}}$. The underlying stellar disk has a smooth, featureless and extended exponential profile, with no features at some radius where the star formation rate or disk instability may be changing properties. If this exponential disk reflects the past history of star formation, then there is no evident threshold.

The stability of galaxy disks is more complicated than what can be captured by this one-dimensional model, however. Stars contribute to the instability, disk thickness impedes it, gas dissipation promotes it, and spirals that fragment into self-gravitating clouds can still form in sub-threshold conditions.

A combined gas+star disk is more unstable than a pure gas disk (Toomre 1964; Jog & Solomon 1984). Romeo & Wiegert (2011) suggest an effective Q_{eff} given by

$$Q_{\text{eff}} = \left(\frac{W}{T_s Q_s} + \frac{1}{T_g Q_g} \right)^{-1} \quad (4)$$

in the likely case where $T_s Q_s > T_g Q_g$, which means that the stellar disk alone is more stable than the gaseous disk alone. Here, $T = 0.8 + 0.7\sigma_z/\sigma_R$ is a thickness correction for gas or stars with velocity dispersions σ in the perpendicular (z) or radial (R) directions. Romeo and Wiegert suggest $\sigma_z/\sigma_R = 0.6$ for stars and 1 for gas, making $T_s = 1.22$ and $T_g = 1.5$. Also, $W = 2\sigma_s\sigma_g/(\sigma_s^2 + \sigma_g^2)$. The quantities T and W depend only on the ratios of velocity dispersions, so a decrease with radius in these dispersions will not affect the results of this discussion. As for the dispersion in Σ_{crit} , the values used in Q_s , Q_g and W are radial components.

Note that $Q_{\text{eff}} < 1$ becomes the instability condition for a 2-fluid thick disk, replacing $Q_g < 1$, or equivalently, $\Sigma_{\text{gas}}/\Sigma_{\text{crit}} > 1$, for the thin disk model discussed above. Thus, we

can convert Q_{eff} to a threshold 2-fluid gas column density for thick disks, $\Sigma_{\text{crit},2\text{F},\text{thick}}$ by setting $Q_{\text{eff}} = 1$ in Eq. 4. We write the 1-fluid critical value for infinitely thin disks that we have been using as $\Sigma_{\text{crit},1\text{F},\text{thin}} = \kappa\sigma_g/(\pi G)$. Then, inverting Eq. 4 and substituting for W , we get

$$\Sigma_{\text{crit},2\text{F},\text{thick}} = \Sigma_{\text{crit},1\text{F},\text{thin}}T_g - \frac{2\Sigma_{\text{star}}T_g}{(1 + \sigma_s^2/\sigma_g^2)T_s} \quad (5)$$

Using the above values for the thickness corrections, T , we get a ratio of observed gas column density to the critical, two-fluid, thick disk column density

$$\frac{\Sigma_{\text{HI+He}}}{\Sigma_{\text{crit},2\text{F},\text{thick}}} = \frac{\Sigma_{\text{HI+He}}/\Sigma_{\text{crit},1\text{F},\text{thin}}}{1.5 - 0.488\Sigma_s/\Sigma_{\text{crit},1\text{F},\text{thin}}}, \quad (6)$$

where we have assumed $\sigma_s/\sigma_g = 2$. Figures 13 and 14 suggest that in the outer disks of our two spiral galaxies, $\Sigma_s \sim \Sigma_g/4$, and Figure 15 indicates that $\Sigma_{\text{HI+He}}/\Sigma_{\text{crit},1\text{F},\text{thin}} \sim 0.2$ or less there. Thus, $\Sigma_s/\Sigma_{\text{crit},1\text{F},\text{thin}} \sim 0.05$, and for this value, the denominator becomes 1.47. Then

$$\frac{\Sigma_{\text{HI+He}}}{\Sigma_{\text{crit},2\text{F},\text{thick}}} \sim 0.68 \frac{\Sigma_{\text{HI+He}}}{\Sigma_{\text{crit},1\text{F},\text{thin}}}. \quad (7)$$

This result means that the 2-fluid thick disk is more stable than the 1-fluid thin disk considered in Figure 15, primarily because of thickness effects, even with the presence of stars. The outer disk is therefore 30% more stable than indicated in Figure 15.

Energy dissipation changes this picture, however. Two-component star+gas thick disks with turbulent gas dissipation (Elmegreen 2011) are more unstable than 2-fluid thick disks that follow the Toomre model, which for gas, assumes an isothermal fluid. For typical conditions in galaxies, instabilities that create star-forming clouds in turbulent gas can occur with average gas column densities as low as 30-50% of the Romeo & Wiegert (2011) critical value given above. This range assumes that turbulent energy dissipates on between 1 and 2 crossing times over the length of the self-gravitational perturbation, and it assumes a ratio of velocity dispersions σ_s/σ_g between 1 and 5. Lower σ_g/σ_s and faster dissipation relative to a crossing time correspond to lower critical gas column densities in the 2-fluid case; i.e., they correspond to greater instability. This factor of 2 or 3 increase in the ratio of the observed $\Sigma_{\text{HI+He}}$ to the threshold column density, now with dissipation included, is still not enough to bring us to an unstable regime in the far outer parts, however.

So far, all of these gravitational instability models apply only to the radial direction, and the instabilities make only rings spaced by the Jeans length. Before a disk becomes this unstable because of radial forcing alone, it becomes unstable to the formation of spiral arms by a combination of radial and azimuthal forcing. Spiral arm formation should always be viewed as the first step in star formation when a disk has shear (which spiral galaxies

have but dIrr galaxies do not). Clouds should not be expected to form directly from the interstellar medium in random places, but they should form as condensations in the spiral arms.

The stability condition for combined radial and azimuthal forcing was written in terms of an effective Q parameter by Lau & Bertin (1978) and Bertin et al. (1989; see also Julian & Toomre 1966),

$$Q_{\text{eff}} = \left(\frac{1}{Q^2} + \frac{J^2 Q^4}{4} \right)^{-1/2} \quad (8)$$

where J is a parameter such that

$$\frac{J^2 Q^4}{4} = (q_t Q)^2 \left(\frac{2\Omega}{\kappa} \right)^2 \left(\left| \frac{d \ln \Omega}{d \ln R} \right| \right) \sim 2 (q_t Q)^2 \quad (9)$$

for rotation rate Ω and dimensionless azimuthal wavenumber $q_t = 2\pi\sigma/(\lambda_t\kappa)$ at wavelength λ_t . The factor 2 in the last expression is for a flat rotation curve. If there are m spiral arms in the azimuthal direction, then $q_t = \sigma m/(\kappa R)$, and if we write $Q = \sigma\kappa/(\pi G\Sigma)$ in the usual way, then $q_t Q = \sigma^2 m/(\pi G\Sigma R) \sim Hm/R$ for scale height H . Condition (8) was applied to disk stability and star formation by Zasov & Simakov (1988). For $\sigma \sim 10 \text{ km s}^{-1}$ and Σ from Figures 13 and 14, we showed above that $H = 13.1 \text{ kpc}$ at $R = 60 \text{ kpc}$ for NGC 801 and $H = 5.7 \text{ kpc}$ at 71 kpc for UGC 2885, respectively, in which case $J^2 Q^4/4 \sim 8(H/R)^2 \sim 0.38$ and 0.05 for $m = 2$. If we now use $\Sigma_{\text{HI+He}}/\Sigma_{\text{crit,1F,thin}} \sim 0.13$ and 0.34 from Figure 15 at these outer radii for the two galaxies, and take 2×0.68 of this ratio for $\Sigma_{\text{HI+He}}/\Sigma_{\text{crit,2F,thick}}$ from equation (7), considering a factor of 2 for turbulence dissipation, then Q , which is the inverse of this ratio, becomes ~ 5.7 for NGC 801 and 2.1 for UGC 2885, which are well in the stable regime. However, the azimuthal force lowers these values considerably, to $Q_{\text{eff}} \sim 1.6$ and 1.9 , respectively. Perhaps as a result of this azimuthal forcing, spiral arms dominate the morphology of star formation even in the outer regions.

The above discussion suggests that for realistic assumptions about the stellar disk thickness and dissipative gas, and with combined radial and azimuthal forcing, the outer regions of our galaxies are marginally unstable to form spirals. Star formation inside of these spirals is greatly aided by the higher local densities. Similarly, Herbert-Fort et al. (2012) suggest that young ($\leq 1 \text{ Gyr}$) clusters formed near the outer edges of galaxy disks are helped by spiral arms. They also note that star clusters much further out, near the HI edge, may have formed as a result of gas accretion from the intergalactic medium. It is possible that multiple factors are responsible for facilitating star formation in the outer disk. In the case of NGC 801, we also cannot rule out gravitational perturbations by the neighboring galaxy as a means of generating spiral arms. Also, propagation of spiral waves from the inner galaxy

could be causing the spiral arms in the outer galaxy without requiring a local mechanism from locally unstable conditions.

4.4. Star formation thresholds

With $H\alpha$, we have azimuthally-averaged star formation profiles to $4R_D$ in NGC 801 and $6R_D$ in UGC 2885, and we have traced exponential stellar disk profiles in both galaxies to the same radii. What is striking is the lack of any disruption in the smooth decline of stellar surface brightness with radius in spite of the highly variable instability parameter Q (see Figure 15). We argued in the previous section that the traditional Q parameter overestimates the stability of the gas, but here we point out that Q really does not seem relevant at all to the stellar disk. There is no change in the exponential profiles; they drop smoothly with radius and with no observed end. Others have also found no correlation between star formation efficiency and Q in inner (Leroy et al. 2008) or outer (Bigiel et al. 2010) spiral disks. Furthermore, the end to $H\alpha$ emission, too, is not likely related to Q , but rather to a lack of detectability, as discussed previously. Earlier inferences of star formation thresholds based on $H\alpha$ emission did not consider the increased difficulty in detecting $H\alpha$ emission in outer disks and since then, FUV emission in spirals has shown that there is star formation in far outer disks, well beyond where $H\alpha$ emission is no longer seen (see, for example, Thilker et al. 2007).

The same situation applies to dwarf galaxies as well, even though their gas disks and Q profiles are even more extreme than in spirals. Our ultra-deep imaging of 5 dIrr galaxies traced the stellar disks to a V -band magnitude of 30 mag arcsec⁻² (Hunter et al. 2011), and several of these galaxies show no change in their exponential profile to that surface brightness. Some dwarfs and spiral galaxies do have breaks in the slopes of their stellar surface brightness profiles (see, for example, Herrmann et al. 2013), but there is no obvious correlation between the radial location of the breaks and a threshold in the Q radial profile.

4.5. Populating the outer disk and disk formation

NGC 801 and UGC 2885 have smooth exponential profiles out to galactocentric distances of at least 60–70 kpc with no apparent cut-off. The H II regions are also observed out this far in these galaxies, although the average surface brightness of $H\alpha$ drops before the optical edge.

The origin of exponential disk profiles is not well understood (van der Kuit & Freeman

2011), and the current observations present severe constraints on any model. The rotation speed in the outer part of NGC 801 is $\sim 220 \text{ km s}^{-1}$ (Rubin et al. 1980), so the orbit time at the outer limit of the exponential disk that we see here, 60 kpc, is 1.7 Gyr. UGC 2885 has an outer disk rotation speed of 300 km s^{-1} (Rubin et al. 1980; Roelfsema & Allen 1985), so at its outer observed limit, 72 kpc, the orbit time is 1.5 Gyr. These times are $\sim 12\%$ of a Hubble time, so the outer disks could have rotated around only ~ 8 times at their greatest possible ages. Any process that forms an exponential disk would have to be faster than this.

The same orbit times are derived for the four galaxies in our deep study of dIrr that have outer disk rotation curves (Hunter et al. 2011), DDO 86: 3.7 Gyr, DDO 133: 1.1 Gyr, NGC 4163: 1.3 Gyr, and IZw 115: 3.0 Gyr. These galaxies also have nearly perfect exponential disks out to the observed edges, where the surface brightness is 30 mag arcsec $^{-2}$ in V -band – fainter than the present observations.

In the outer regions of our spiral galaxies, $\Sigma_{\text{total}} \sim 1 M_{\odot} \text{ pc}^{-2}$ (Figures 13 and 14), so if the perpendicular velocity dispersion is $\sigma \sim 10 \text{ km s}^{-1}$, then the crossing time through the disk is $\sigma/(\pi G \Sigma_{\text{total}}) \sim 720 \text{ Myr}$. A complete cycle perpendicular to the disk involves 4 of these crossings of a scale height each, so the time is again $\sim 3 \text{ Gyr}$.

The dynamical time for star formation is also about the disk crossing time, i.e., several hundred Myr in the far-outer disks studied here. Thus, we have outer disk star formation that appears analogous to inner disk star formation except for an extremely low average rate. The average rate decreases with radius by nearly 3 orders of magnitude if we scale it to the surface brightness. One order of magnitude of this decrease is because the dynamical time is longer in the outer part, another order of magnitude is because the total gas surface density is lower in the outer part, and a third order of magnitude is because the fraction of the gas that is molecular is lower in the outer part if the areal star formation rate is proportional to the molecular column density.

It seems baffling how the average star formation rate can maintain such a precise exponential disk for 3 orders of magnitude in both dIrr galaxies and these spiral galaxies. This is especially puzzling when the molecular fraction is only a small part of the gas: how do molecular clouds forming at extremely low rates know what the rest of the galaxy is doing? The orbit time varies with radius like a power law ($1/R$) while the perpendicular oscillation time or disk crossing time, which is approximately the turbulent dissipation time, increases exponentially with radius for a fixed velocity dispersion. In the inner disk, the perpendicular crossing time is much less than the orbit time, but in the outer disk these times are about the same. The Toomre model has a characteristic timescale comparable to the epicyclic time, which is about the orbit time, whereas cloud formation that combines gas dissipation and local stellar dynamics has a timescale somewhat between the orbit and crossing times. If these

times vary separately with radius, then how do the cloud formation rate and internal cloud evolution rate combine to give a star formation rate that ends up precisely exponential?

If only the perpendicular crossing time mattered for star formation, because the most important processes are governed by dissipation, for example, then the exponential can be self-sustaining: once the disk has an exponential dependence on radius, then the perpendicular crossing time is exponential, and star formation following this crossing time would also be exponential. This situation could be stabilized in the short term by feedback, which puffs up the disk when the star formation rate is too high and makes the crossing time longer. But it would seem to be unstable in the long term for a given average velocity dispersion because a high star formation rate in some annulus would make the disk relatively dense there, and this would lower the local crossing time and speed up the star formation, making the disk even denser. Subsequent smoothing by stellar spirals (Sellwood & Binney 2002) could recover the original exponential. The same instability would seem to arise in more detailed models, such as that by Ostriker et al. (2010), in which the star formation rate per unit area scales with the gas column density multiplied by the square root of the local midplane stellar volume density. If the long-term star formation rate increases with background stellar density, then the exponential profile would seem to be unstable.

We are left with a choice between two puzzling models: (1) the molecular cloud and star formation rates have an exponential profile independent of the underlying stars and this rate profile forces the stellar disk to build up such a profile too, or, (2) the stellar disk is continuously adjusted to an exponential shape regardless of the star formation profile, and then star formation tends to follow the existing stars for dynamical reasons and occasional sequential triggering. However, the latter seems more reasonable at the present time because global dynamical processes can be imagined which scatter the stars and keep the disk globally exponential. Stellar waves might do this (Roskar et al. 2008), although dwarf irregulars have extended exponentials with no obvious waves. Initial conditions that are exponential (Mestel 1963, van der Kruit 1987) do not help solve this problem because in the present models of galaxy formation, disk mass is added by gas accretion over a long period of time with in situ star formation playing a decisive role in the distribution of new stars. In both of these models, the star formation profile does not follow the gas in the outer parts, which is mostly H I.

5. Conclusions

We have examined star formation in two very luminous ($M_V = -22$ to -23) Sc-type spiral galaxies, NGC 801 and UGC 2885, using ultra-deep H α images. We combine these with

UBV and 2MASS *JHK* images and H I maps to explore the star formation characteristics of disk galaxies at high luminosity.

H α traces star formation in these galaxies to 4-6 disk scale lengths. We find that the most distant H II regions are found at the tips of spiral arms: at radii of $3.9R_D$ and $5.6R_D$ and local H I densities of $1.5 M_\odot \text{ pc}^{-2}$ and $6 M_\odot \text{ pc}^{-2}$, for NGC 801 and UGC 2885, respectively. In UGC 2885 there are also a few identifiable detached H II regions as far out as $6.1R_D$ at $2.3 M_\odot \text{ pc}^{-2}$.

Except in the center ($R < 1.8R_D$) of NGC 801, the azimuthally-averaged current SFR is lower than the SFR necessary to form the stellar mass over the lifetime of the galaxy and the current SFR is particularly low in the outer disks. However, the decrease in current SFR relative to that in the past is not consistent with the relatively constant colors in the outer disks. The lack of detection of H α further out is likely due to loss of Lyman continuum photons, and stellar migration processes may also be important in populating the outer disk.

The gas in the outer regions is marginally stable to gravitational instabilities in an average sense, and star formation is taking place in regions of locally higher gas densities, namely, spiral arms. The traditional Toomre (1964) gravitational instability parameter Q is everywhere larger than 1, implying a stable gas. However, when we include the stellar disk thickness with dissipative gas and both radial and azimuthal forcing (Q_{eff}), the outer regions become marginally unstable to form spiral arms. Star formation occurs in these arms with higher local densities than the surrounding average. Generally spirals grow at higher Q than the radial stability threshold, so the spirals are the primary instability, from which star formation follows at the locally increased densities in the arms.

We have traced smooth exponential stellar disks over 3-orders of magnitude and 4-6 disk scale lengths, in spite of a highly variable gravitational instability parameter. Thus, gravitational instability thresholds do not seem relevant to the stellar disk. One possibility for creating an exponential disk is that the star formation activity has an exponential profile and this forces the stellar disk to build up such a profile too. Another possibility is that the stellar disk is continuously adjusted to an exponential shape regardless of the star formation profile. The latter could be due to global dynamical processes that scatter the stars. However, the known scattering processes only operate in spiral systems and cannot explain the same situation of smooth exponential disks observed in dIrr galaxies. Perhaps clumps in dIrr galaxies play the role of scattering centers to make the disks exponential (Hunter et al. 2011).

We are grateful to J. M. van der Hulst for help in retrieving the H I data of UGC 2885 from the WHISP archives. The WHISP observation were carried out with the Westerbork

Synthesis Radio Telescope, which is operated by the Netherlands Foundation for Research in Astronomy (ASTRON) with financial support from the Netherlands Foundation for Scientific Research (NWO). The WHISP project was carried out at the Kapteyn Astronomical Institute by J. Kamphuis, D. Sijbring and Y. Tang under the supervision of T. S. van Albada, J. M. van der Hulst and R. Sancisi. Support for this work was provided to DAH by the Mt. Cuba Astronomical Foundation and by grant AST-0707563 from the National Science Foundation. BGE received support from National Science Foundation grant AST-0707426. AA and TW are grateful for participation in the Northern Arizona University Research Experiences for Undergraduates program in the summers of 2012 and 2010. This program is run by Dr. Kathy Eastwood and funded by the National Science Foundation through grant AST-1004107. This research has made use of NED which is operated by the Jet Propulsion Laboratory, California Institute of Technology, under contract with the National Aeronautics and Space Administration.

Facilities: Hall 1.1 m, KPNO, WSRT

REFERENCES

- Asplund, M., Grevesse, N., Sauval, A. J., & Scott, P. 2009, *ARA&A*, 47, 481
- Barker, M. K., Ferguson, A. M. N., Irwin, M. J., Arimoto, N., & Jablonka, P. 2012, *MNRAS*, 419, 1489
- Barnes, K. L., van Zee, L., Côté, S., & Schade, D. 2012, *ApJ*, 757, 64
- Beckman, J. E., Rozas, M., Zurita, A., Watson, R. A., & Knapen, J. H. 2000, *AJ*, 119, 2728
- Bell, E. F., & de Jong, R. S. 2000, *MNRAS*, 312, 497
- Bertin, G., Lin, C. C., Lowe, S. A., & Thurstans, R. P. 1989, *ApJ*, 338, 104
- Bigiel, F., Leroy, A., Walter, F., Brinks, E., de Blok, W. J. G., et al. 2008, *AJ*, 136, 2846
- Bigiel, F., Leroy, A., Walter, F., Blitz, L., Brinks, E., de Blok, W. J. G., & Madore, B. 2010, *AJ*, 140, 1194
- Bland-Hawthorn, J., Vlajić, M., Freeman, K. C., & Draine, B. T. 2005, *ApJ*, 629, 239
- Bossier, S., Gil de Paz, A., Boselli, A., Madore, B. F., Buat, V., et al. 2007, *ApJS*, 173, 524
- Brinchmann, J., Charlot, S., White, S. D. M., et al. 2004, *MNRAS*, 351, 1151

- Burstein, D., Rubin, V. C., Thonnard, N., & Ford, W. K., Jr. 1982, *ApJ*, 253, 70
- Calzetti, D. 1997, in *AIP Conf. Proc.* 408, *The Ultraviolet Universe at Low and High Redshift : Probing the Progress of Galaxy Evolution*, eds. W. H. Waller, M. N. Fanelli, J. E. Hollis, & A. C. Danks (Woodbury:AIP), 403
- Calzetti, D., Armus, L., Bohlin, R. C., Kinney, A. L., Koornneef, J., & Storchi-Bergmann, T. 2000, *ApJ*, 533, 682
- Calzetti, D., Kinney, A. L., & Storchi-Bergmann, T. 1994, *ApJ*, 429, 582
- Cardelli, J. A., Clayton, G. C., & Mathis, J. S. 1989, *ApJ*, 345, 245
- Carraro, G., Vázquez, R. A., Costa, E., Perren, G., & Moitinho, A. 2010, *ApJ*, 718, 683
- Chang, R. X., Shen, S. Y., & Hou, J. L. 2012, *ApJL*, 753, id L10
- Chiappini, C., Matteucci, F., & Gratton, R. 1997, *ApJ*, 477, 765
- Christlein, D., Zaritsky, D., & Bland-Hawthorn, J. 2010, *MNRAS*, 405, 2549
- de Vaucouleurs, G., & de Vaucouleurs, A. 1972, *Memoirs of the Royal Astronomical Society*, Vol 77, p 1
- de Vaucouleurs, G., de Vaucouleurs, A., Corwin, H., Buta, R., Paturel, G., & Fouqué, P. 1991, *Third Reference Catalogue of Bright Galaxies (New York, Springer-Verlag) (RC3)*
- Elmegreen, B. G. 2011, *ApJ*, 737, 10
- Espada, D., Muñoz-Mateos, J. C., Gil de Paz, A., et al. 2011, *ApJ*, 736, 20
- Eufrazio, R. T., de Mello, D. F., Urrutia-Viscarra, F., de Oliveira, C. M., & Dwek, E. 2013, in *Proceedings of the International Astronomical Union, Volume 8, Symposium S292, “Molecular Gas, Dust, and Star Formation in Galaxies,”* p 328
- Ferguson, A. M. N., & Johnson, R. A. 2001, *ApJ*, 559, L13
- Ferguson, A. M. N., Wyse, R. F. G., Gallagher, J. S., & Hunter, D. A. 1998, *ApJ*, 506, 19
- Grossi, M., Hwang, N., Corbelli, E., Giovanardi, C., Okamoto, S., & Arimoto, N. 2011, *A&A*, 533, A91
- Henry, R. B. C., & Worthey, G. 1999, *PASP*, 111, 919

- Herbert-Fort, S., Zaritsky, D., Moustakas, J., Di Paola, A., Pogge, R. W., & Ragazzoni, R. 2012, *ApJ*, 754, id 110
- Herrmann, K. A., Hunter, D. A., & Elmegreen, B. G. 2013, *AJ*, submitted
- Holwerda, B. W., González, R. A., van der Kruit, P. C., & Allen, R. J. 2005, *A&A*, 444, 109
- Huizinga, J. E. & van Albada, T. S., 1992, *MNRAS*, 254, 677
- Hunter, D. A. 1982, *ApJ*, 260, 81
- Hunter, D. A., Elmegreen, B. G., & Ludka, B. C. 2010, *AJ*, 139, 447
- Hunter, D. A., Elmegreen, B. G., Oh, S.-H., et al. 2011, *AJ*, 142, 121
- Hunter, D. A., & Gallagher, J. S., III 1986, *PASP*, 98, 5
- James, P. A., Shane, N. S., Knapen, J. H., Etherton, J., Percival, S. M. 2005, *A&A*, 429, 851
- Jog, C. J., & Solomon, P. M. 1984, *ApJ*, 276, 114
- Julian, W. H., & Toomre, A. 1966, *ApJ*, 146, 810
- Kamphuis, J., & Sancisi, R. 1993, *A&A*, 273, L31
- Kennicutt, R. C., Jr. 1984, *ApJ*, 287, 116
- Kennicutt, R. C., Jr. 1998, *ARAA*, 36, 189
- Kennicutt, R. C., Jr. 1989, *ApJ*, 344, 685
- Kennicutt, R. C., Jr., Calzetti, D., Walter, F. et al. 2007, *ApJ*, 671, 333
- Landolt, A. U. 1992, *AJ*, 104, 340
- Larson, R. B. 1976, *MNRAS*, 176, 31
- Lau, Y. Y., & Bertin, G. 1978, *ApJ*, 226, 508
- Lee, J. H., Hwang, N., & Lee, M. G. 2011, *ApJ*, 735, 75
- Leitherer, C., Schaerer, D., Goldader, J. D., González Delgado, R. M., Robert, C., et al. 1999, *ApJS*, 123, 3
- Leroy, A. K., Walter, F., Brinks, E., et al. 2008, *ApJ*, 136, 2782

- Mestel, L. 1963, MNRAS, 126, 553
- Mo, H. J., Mao, S., & White, S. D. M. 1998, MNRAS, 295, 319
- Naab, T. & Ostriker, J. P. 2006, MNRAS, 366, 899
- Osterbrock, D. E. 1989, *Astrophysics of Gaseous Nebulae and Active Galactic Nuclei* (Mill Valley, California:University Science Books)
- Ostriker, E. C., McKee, C. F., & Leroy, A. K. 2010, ApJ, 721, 975
- Patterson, M. T., Walterbos, R. A. M., Kennicutt, R. C., Chiappini, C., & Thilker, D. A. 2012, MNRAS, 422, 401
- Pellegrini, E. W., Oey, M. S., Winkler, P. F., et al. 2012, ApJ, 755, 40
- Pilyugin, L. S., Thuan, T. X., & Vlchez, J. M. 2007, MNRAS, 375, 353
- Prescott, M. K. M., Kennicutt, R. C., Jr., Bendo, G. J., et al. 2007, ApJ, 668, 182
- Quirk, W. J. 1972, ApJL, 176, L9
- Radburn-Smith, D. J., Roškar, R., Debattista, V. P., Dalcanton, J. J., Streich, D., de Jong, R.S., Vlajic, M., Holwerda, B.W., Purcell, C.W., Dolphin, A.E., & Zucker, Daniel B. 2012, ApJ, 753, 138
- Relaño, M., Kennicutt, R. C., Jr., Eldridge, J. J., Lee, J. C., & Verley, S. 2012, MNRAS, 423, 2933
- Roediger, J. C., Courteau, S., Sánchez-Blázquez, P., & McDonald, M. 2012, ApJ, 758, 41
- Roelfsema, P. R., & Allen, R. J. 1985, A&A, 146, 213
- Romeo, A. B., & Wiegert, J. 2011, MNRAS, 416, 1191
- Roškar, R., Debattista, V. P., Stinson, G. S., Quinn, T. R., Kaufmann, T., & Wadsley, J. 2008, ApJ, 675, L65
- Roškar, R., Debattista, V. P., Quinn, T. R., Stinson, G. S., & Wadsley, J. 2008, ApJ, 684, L79
- Rubin, V. C., Ford, W. K. Jr., & Thonnard, N. 1980, ApJ, 238, 471
- Ryder, S. D., & Dopita, M. A. 1994, ApJ, 430, 142

- Saha, A., et al. 2010, *AJ*, 140, 1719
- Salpeter, E. E. 1955, *ApJ*, 121, 161
- Sault, R. J., Teuben, P. J., & Wright, M. C. H. 1995, in *ASP Conference Series Vol 77, Astronomical Data Analysis Software and Systems IV*, eds. R. A. Shaw, H. E. Payne, & J. J. E. Hayes (San Francisco:Astronomical Society of the Pacific), p 433
- Schlaflty, E. F. & Finkbeiner, D. P. 2011, *ApJ*, 737, 103
- Schlegel, D. J., Finkbeiner, D. P., & Davis, M. 1998, *ApJ*, 500, 525
- Sellwood, J. A., & Binney, J. J. 2002, *MNRAS*, 336, 785
- Tamburro, D., Rix, H.-W., Leroy, A. K., et al. 2009, *AJ*, 137, 4424
- Thilker, D. A., Bianchi, L., Boissier, S., Gil de Paz, A., Madore, B. F., et al. 2005, *ApJ*, 619, L79
- Thilker, D. A., Bianchi, L., Meurer, G., Gil de Paz, A., Boissier, S., et al. 2007, *ApJS*, 173, 538
- Toomre, A. 1964, *ApJ*, 139, 1217
- van der Hulst, J. M., van Albada, T. S., & Sancisi, R. in *ASP Conference Proceedings Vol 240, Gas and Galaxy Evolution*, eds. J. E. Hibbard, M. Rupen, & J. H. van Gorkom (San Francisco:Astronomical Society of the Pacific), p 451
- van der Kruit, P. C. 1987, *A&A*, 173, 59
- van der Kruit, P. C., & Freeman, K. 2011, *ARA&A*, 49, 301
- Vlajić, M., Bland-Hawthorn, J., & Freeman, K. C. 2009, *ApJ*, 697, id 361
- Vlajić, M., Bland-Hawthorn, J., & Freeman, K. C. 2011, *ApJ*, 732, id 7
- Vogelaar, M. G. R., & Terlouw, J. P. 2001, in *Astronomical Data Analysis Software Systems I*, eds D. M. Worall, C. Biemesderfer, and J. Barnes, *ASP Conference Serices No. 25*, p 131
- Wang, B., & Heckman, T. M., 1996, *ApJ*, 457, 645
- Wang, J., Kauffmann, G., Józsa, G. I. G., et al. 2013, *MNRAS*, submitted
- Yoachim, P., Roškar, & Debattista, V. P. 2012, *ApJ*, 752, id 97

Zasov, A. V., & Simakov, S. G. 1988, *Astrophysics*, 29, 518

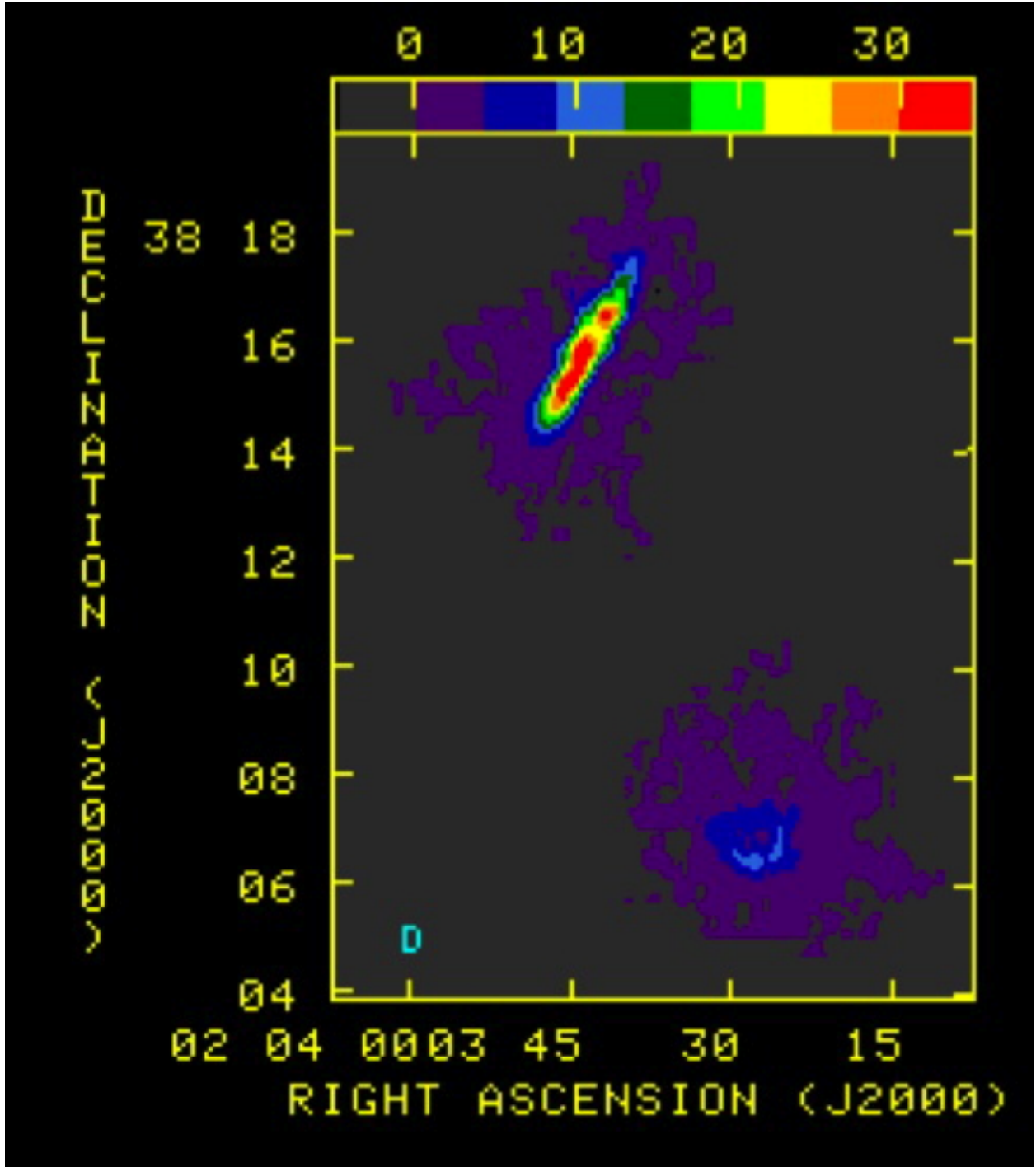


Fig. 1.— False color image of the integrated HI map of NGC 801. NGC 801 is to the northeast and NGC 797 is the galaxy to the southwest. The two galaxies are 110 km s^{-1} and 215 kpc apart at a distance of 79.4 Mpc. The beam FWHM is shown in the lower left. The color bar is in units of WU, which is 5 mJy beam^{-1} , and 1 WU here corresponds to $1.05 \times 10^{20} \text{ atoms cm}^{-2}$.

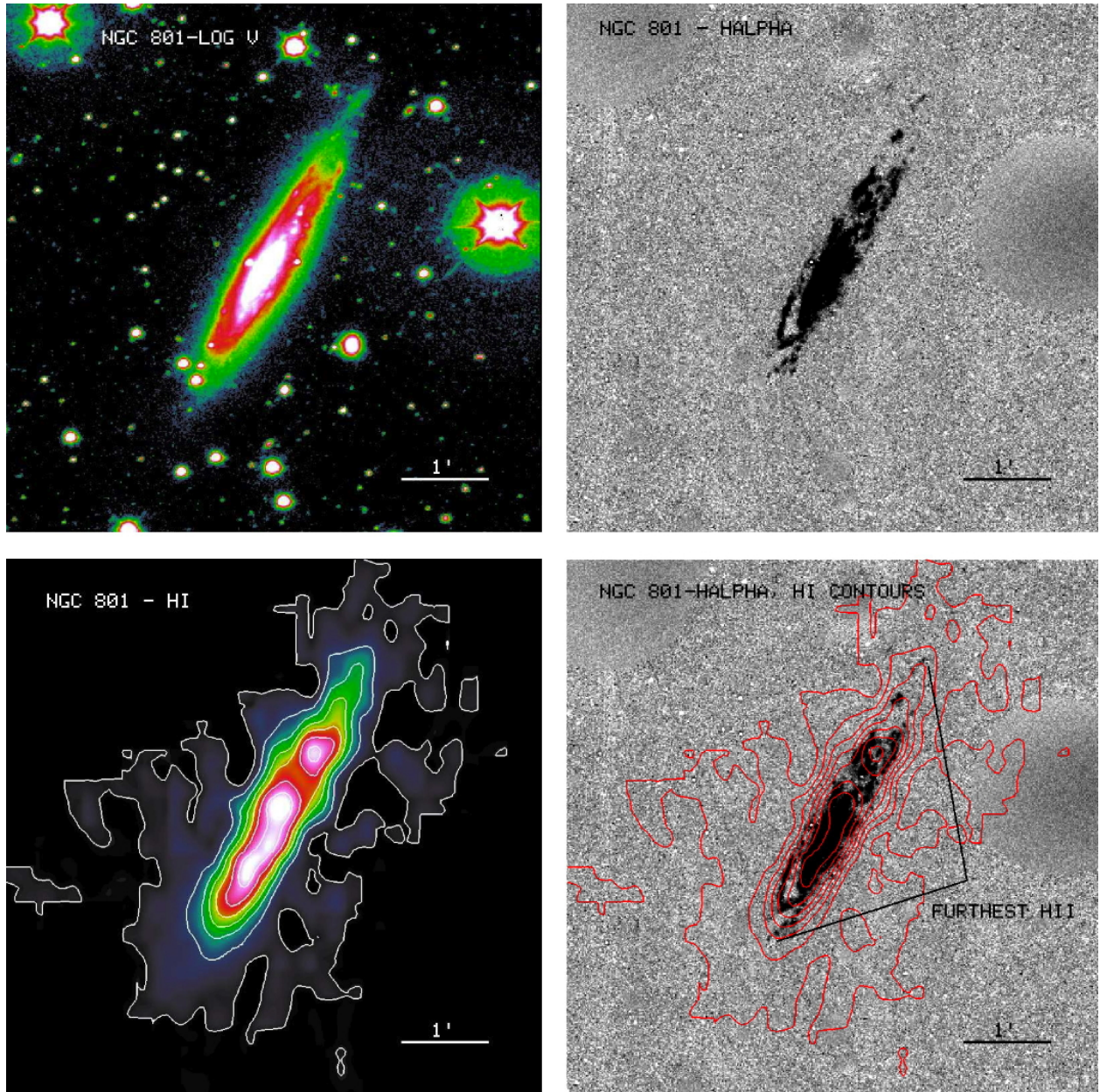


Fig. 2.— Images of NGC 801. All images show the same field of view. *Upper left*: V-band shown in false-color as the logarithm in order to allow inner details to be seen. *Upper right*: H α image with stellar continuum subtracted to leave only nebular emission. *Lower left*: Integrated H I map in false-color with contours superposed. The beam size is $16.1'' \times 27.0''$. *Lower right*: H α image with integrated H I contours superposed. The contours begin at $4.2 \times 10^{19} \text{ cm}^{-2}$ and increase in steps of $5.2 \times 10^{20} \text{ cm}^{-2}$. The location of distant H II regions are marked.

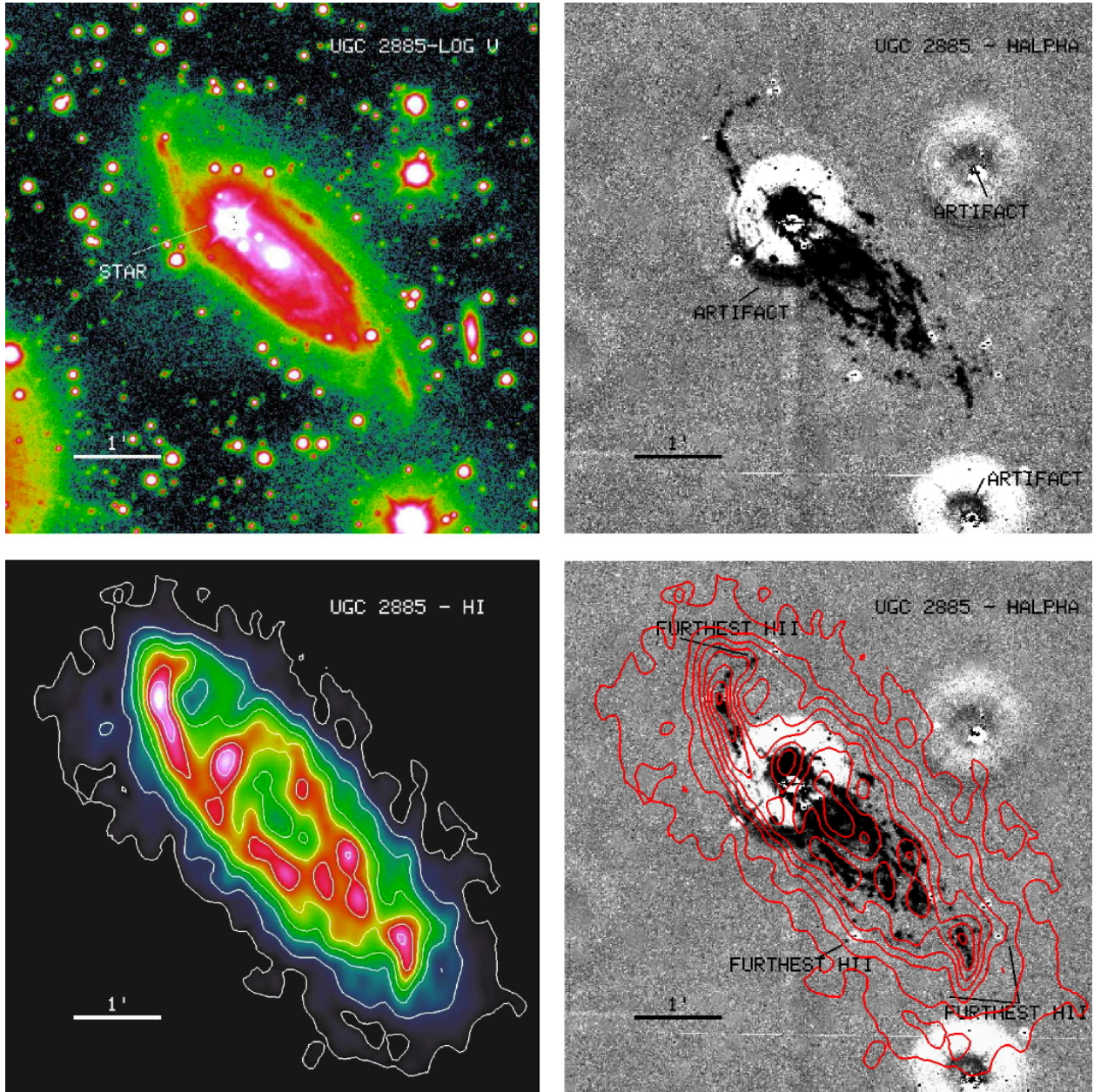


Fig. 3.— Images of UGC 2885. All images show the same field of view. *Upper left*: V-band shown in false-color as the logarithm in order to allow inner details to be seen. *Upper right*: H α image with stellar continuum subtracted to leave only nebular emission. Artifacts due to poor subtraction of saturated stars are marked. *Lower left*: Integrated HI map in false-color with contours superposed. The beam size is $22.27'' \times 13.58''$. *Lower right*: H α image with integrated HI contours superposed. The contours begin at $4.2 \times 10^{19} \text{ cm}^{-2}$ and increase in steps of $5.2 \times 10^{20} \text{ cm}^{-2}$, as for NGC 801. The location of distant H II regions are marked.

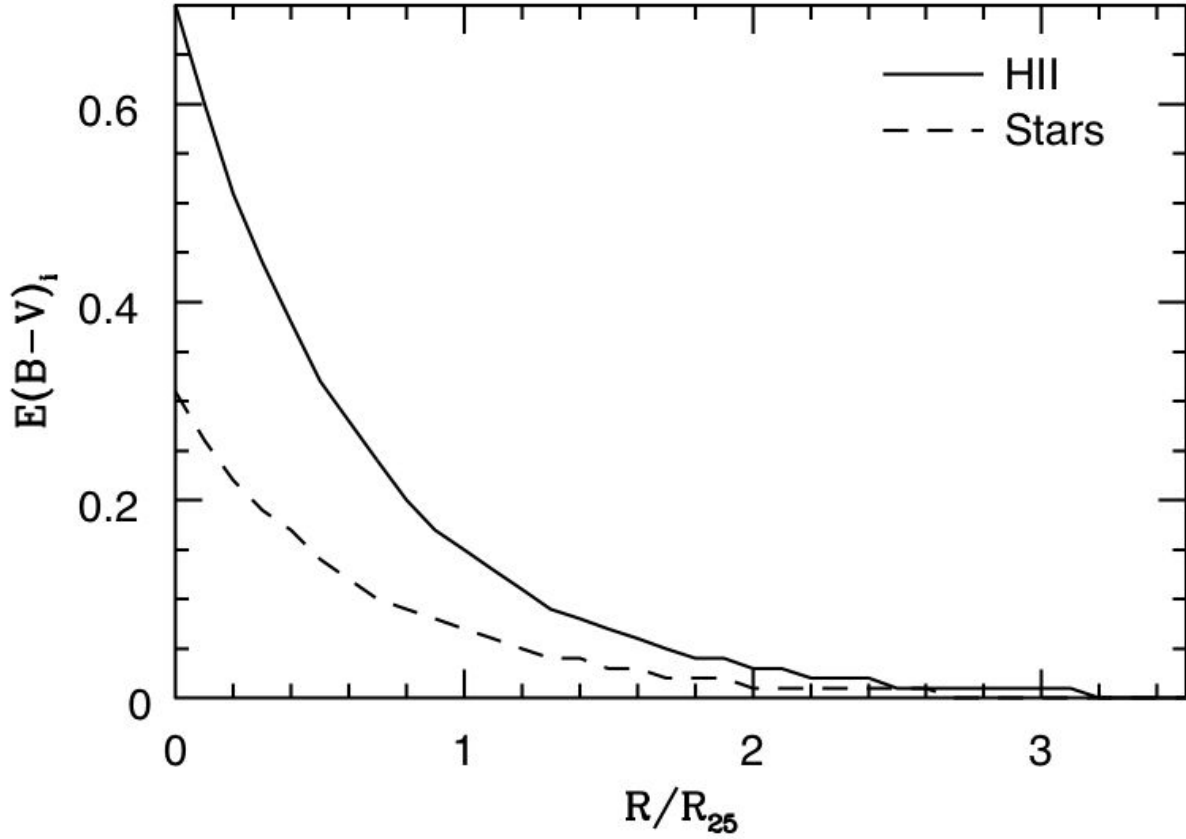


Fig. 4.— Internal reddening $E(B-V)_i$ as a function of radius, adopted and extrapolated from Prescott et al. (2007). This is appropriate for H II regions, and hence our $H\alpha$ observations. For the field stars we adopt a scaling factor of 0.44 times $E(B-V)_i$ for the H II regions (Calzetti 1994).

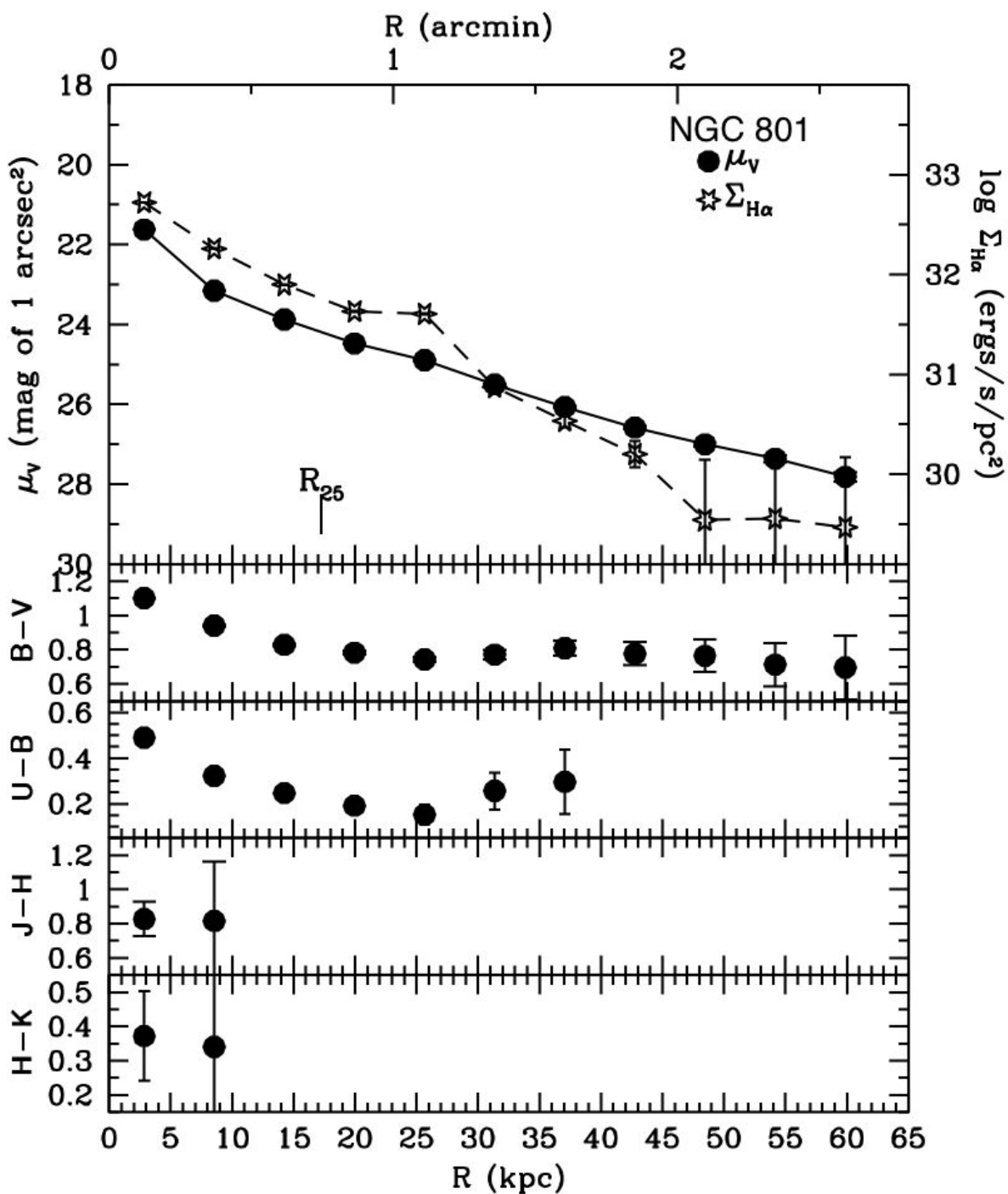


Fig. 5.— Surface photometry and colors of NGC 801 from $UBVJHK$ and $H\alpha$ images. The photometry has not been corrected for reddening. R_{25} is the radius of the galaxy at the B -band surface brightness of 25 mag of 1 arcsec².

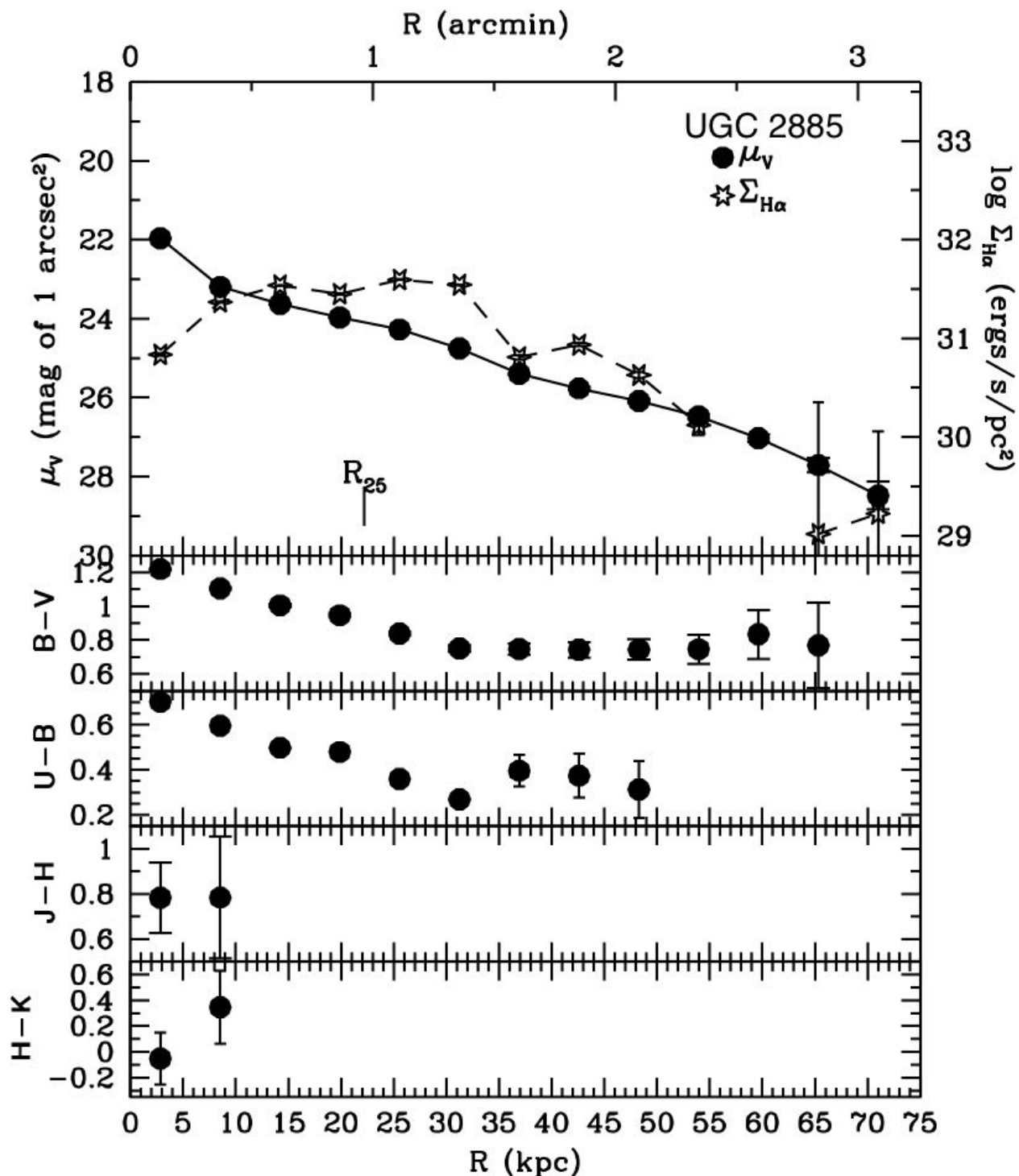


Fig. 6.— Surface photometry and colors of UGC 2885 from $UBVJHK$ and $H\alpha$ images. There is no emission in the third to last annulus (60 kpc radius) in the azimuthally-average $H\alpha$ photometry; hence, there is a discontinuity in the $H\alpha$ profile. The photometry has not been corrected for reddening. R_{25} is the radius of the galaxy at the B -band surface brightness of 25 mag of 1 arcsec².

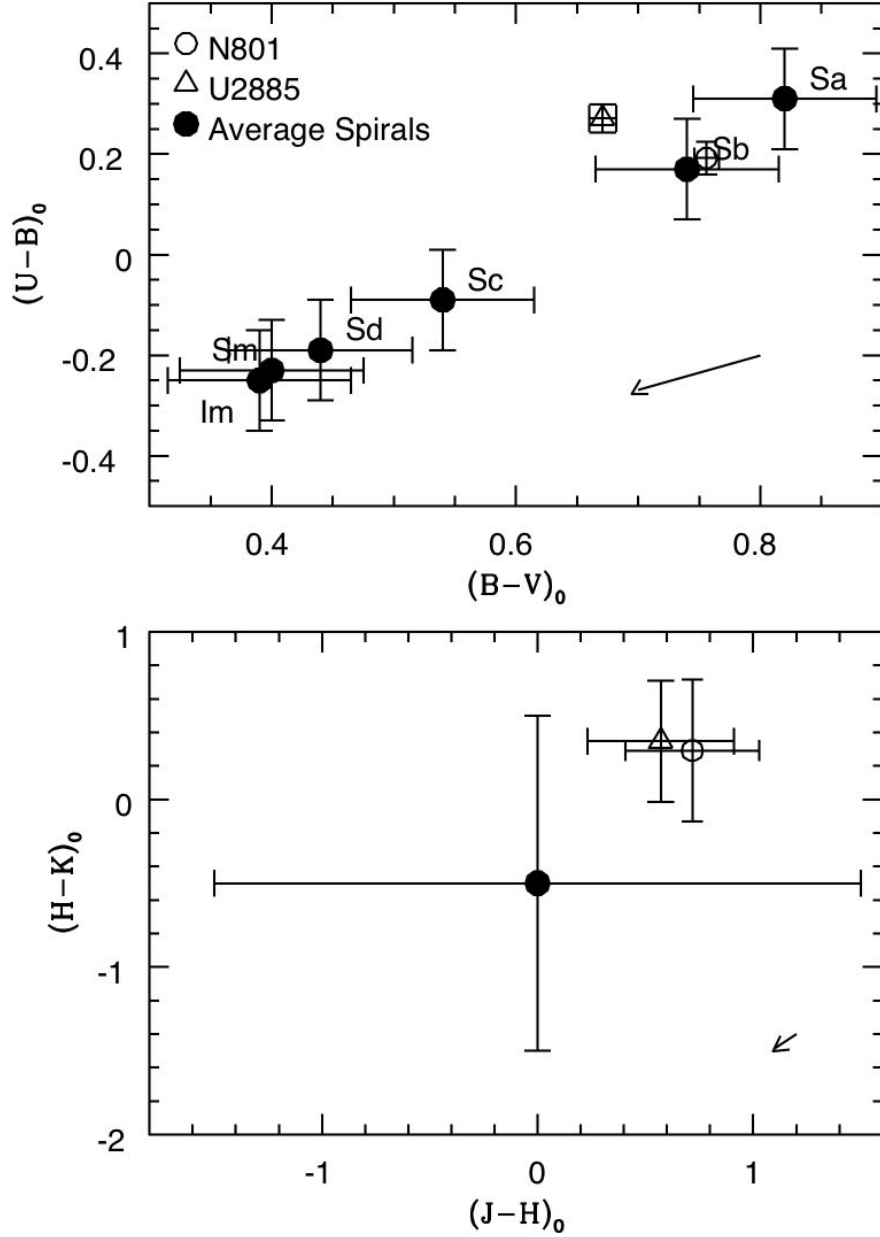


Fig. 7.— Comparison of NGC 801 and UGC 2885 integrated colors to averages for spirals. *Upper panel:* *UBV* color-color diagram. Averages by spiral morphological type are from de Vaucouleurs & de Vaucouleurs (1972). The uncertainties are the spread in colors for each type. The arrow shows the reddening vector for $E(B-V)=0.1$. UGC 2885 is redder than other Sc-type galaxies, and NGC 801 has colors comparable to typical Sb-type systems. *Lower panel:* *JHK* color-color diagram. The large black point is the average for spiral disks from Holwerda et al. (2005), and the uncertainties are the range of values. The arrow is the reddening vector for $E(J-H)=0.1$. NGC 801 and UGC 2885 are redder than most other spirals but within the range of values seen.

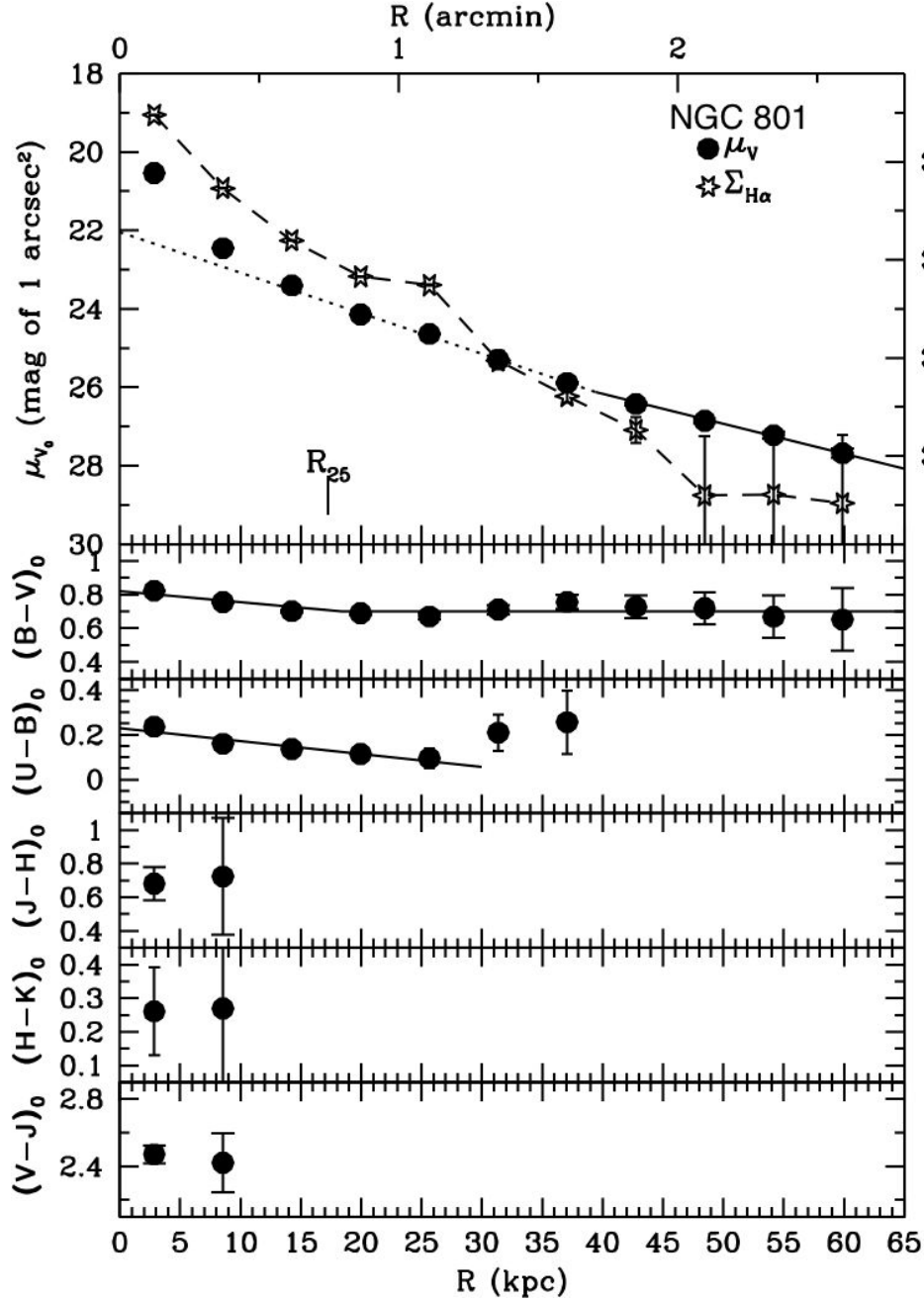


Fig. 8.— Azimuthally-averaged surface photometry and colors of NGC 801 from *UBVJHK* and $H\alpha$ images, corrected for reddening. R_{25} is the radius of the galaxy at the B -band surface brightness of 25 mag of 1 arcsec². The dotted black line in the upper panel is the fit to the inner V -band surface brightness profile, and the solid line is the fit to the outer profile. The inner component has a disk scale length of 10.5 ± 0.4 kpc and a central surface brightness of 22.0 ± 0.1 mag of 1 arcsec². The outer component has a disk scale length of 14.1 ± 0.5 kpc and a central surface brightness of the disk of 23.1 ± 0.1 mag of 1 arcsec². The solid lines in the *UBV* color panels represent a fit to the data: the first 5 points [$(B-V)_0 = 0.82 \pm 0.02 - (0.0065 \pm 0.001) \times R(\text{kpc})$, $(U-B)_0 = 0.23 \pm 0.02 - (0.0058 \pm 0.001) \times R(\text{kpc})$], and in the case of $(B-V)_0$ points 5-11 (constant at 0.70 ± 0.01).

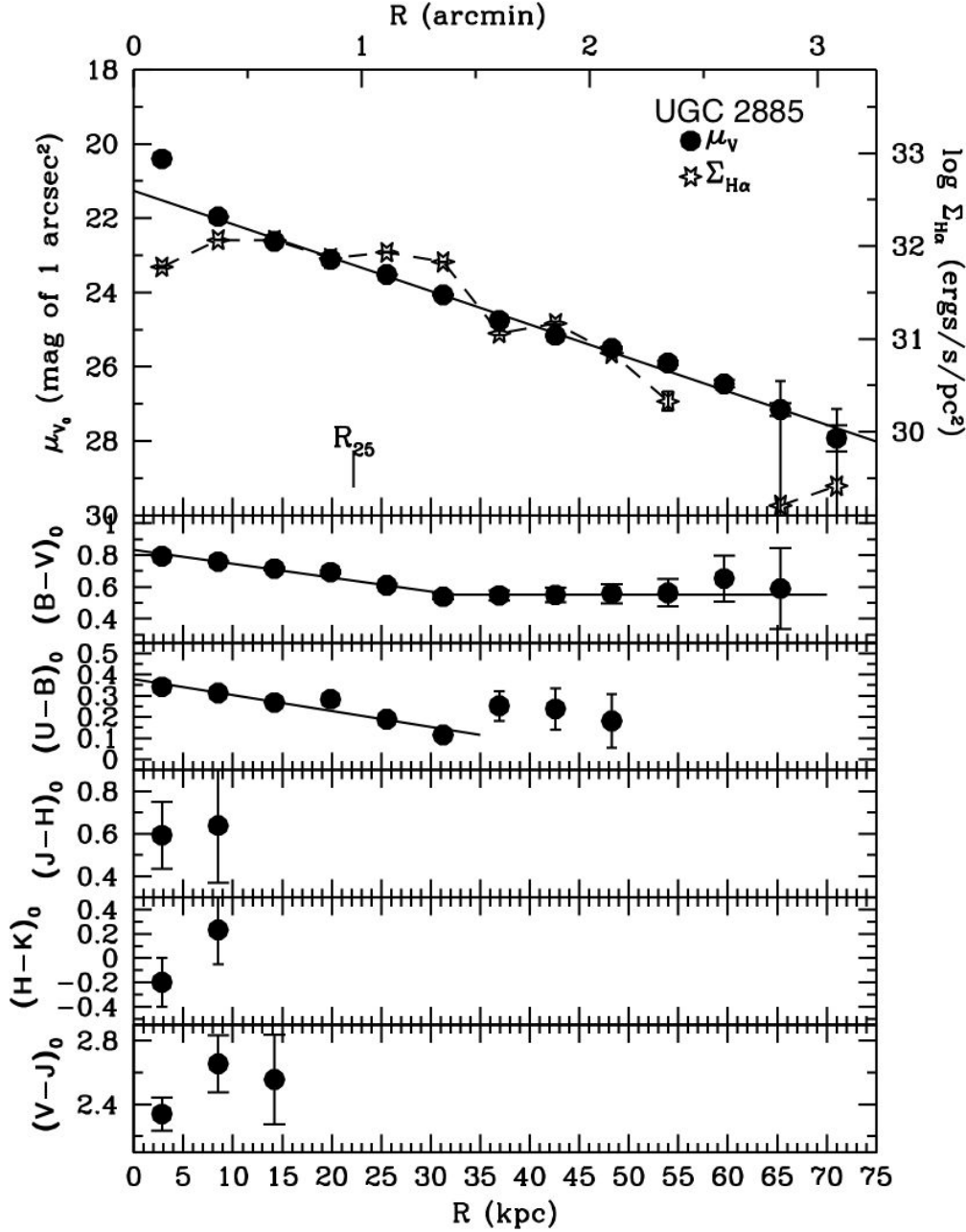


Fig. 9.— Azimuthally-averaged surface photometry and colors of UGC 2885 from $UBVJHK$ and $H\alpha$ images, corrected for reddening. There is no emission in the third to last annulus (60 kpc radius) in the azimuthally-average $H\alpha$ photometry; hence, there is a discontinuity in the $H\alpha$ profile. R_{25} is the radius of the galaxy at the B -band surface brightness of 25 mag of 1 arcsec². The solid black line in the upper panel is the fit to the outer V -band surface brightness profile. This yields a disk scale length of 12.05 ± 0.41 kpc and a central surface brightness of the disk of 21.26 ± 0.15 mag of 1 arcsec². The solid lines in the UBV color panels represent a fit to the data: the first 6 points ($(B-V)_0 = 0.83 \pm 0.02 - (0.0087 \pm 0.001) \times R(\text{kpc})$, $(U-B)_0 = 0.38 \pm 0.03 - (0.0075 \pm 0.001) \times R(\text{kpc})$], and in the case of $(B-V)_0$ points 6-10 (constant at 0.55 ± 0.004).

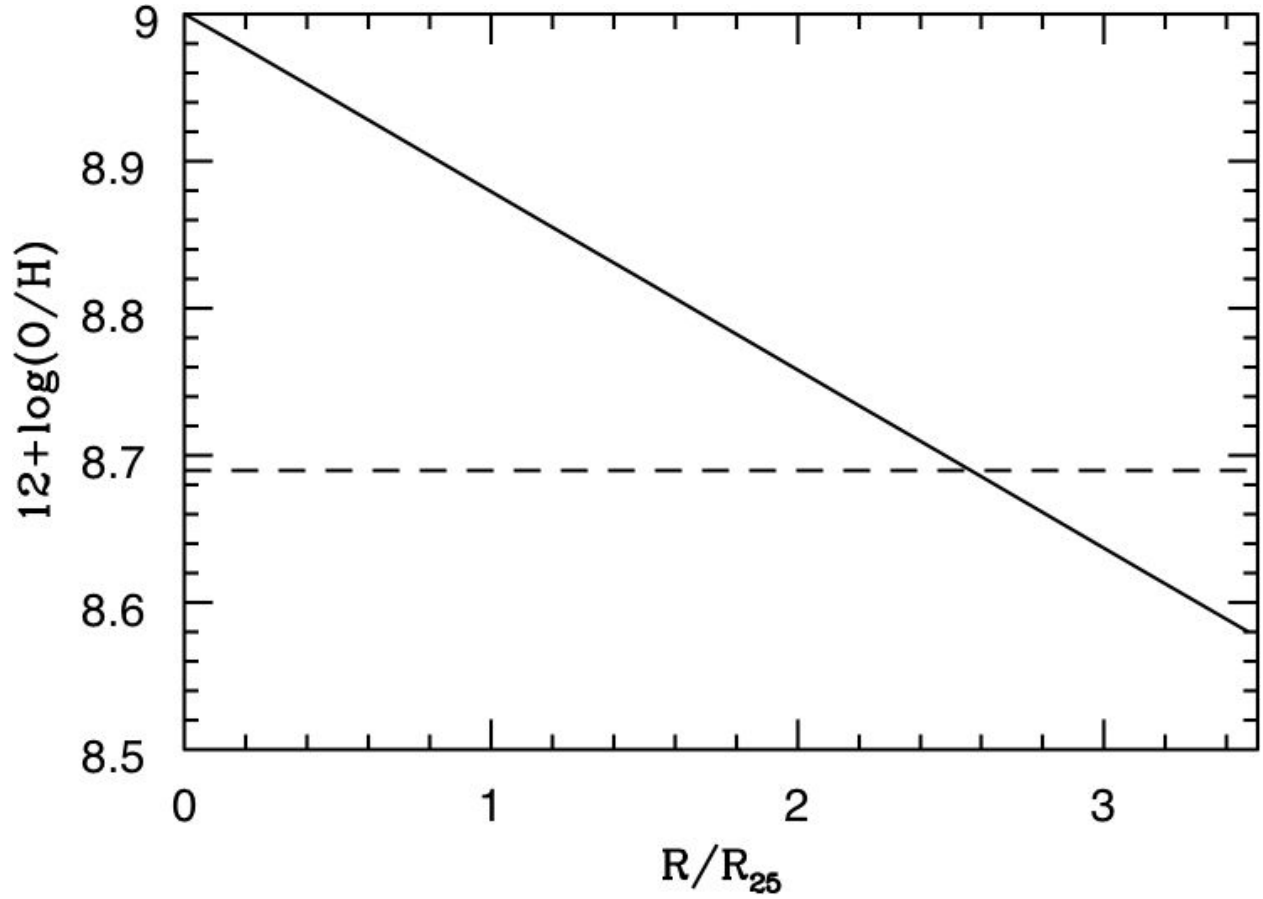


Fig. 10.— Oxygen abundance as a function of radius adopted from Patterson et al. (2012) for M81 and extrapolated to our radial extent. The dashed horizontal line marks the solar abundance of 8.69 (Asplund et al. 2009).

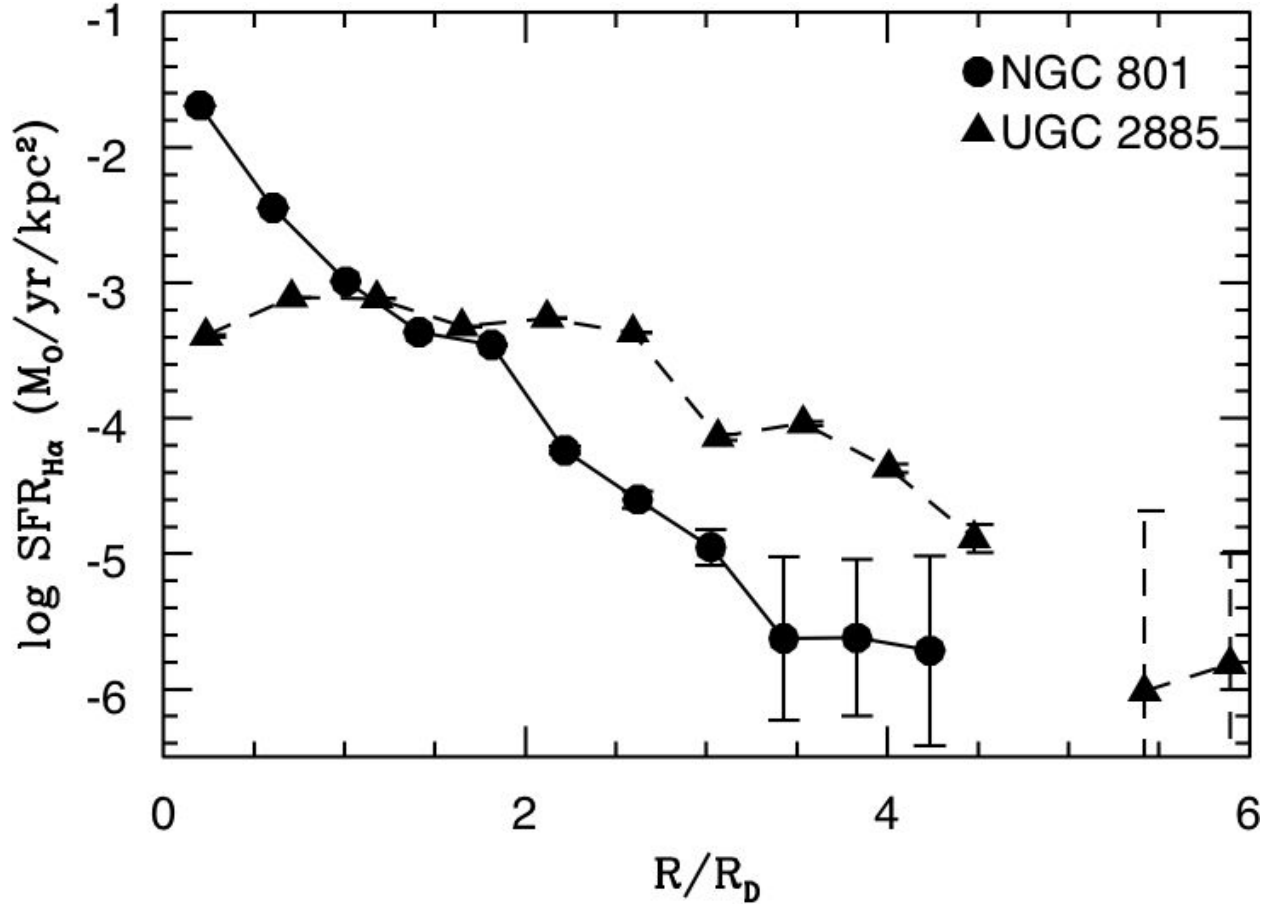


Fig. 11.— $H\alpha$ -derived SFRs for NGC 801 and UGC 2885, where the formula for converting $H\alpha$ surface photometry to $\text{SFR}_{H\alpha}$ is modified for the abundance gradient adopted in Figure 10. For UGC 2885, there is no $H\alpha$ emission in the third to last azimuthally-averaged annulus (60 kpc radius); hence, there is a discontinuity in the $\text{SFR}_{H\alpha}$ profile.

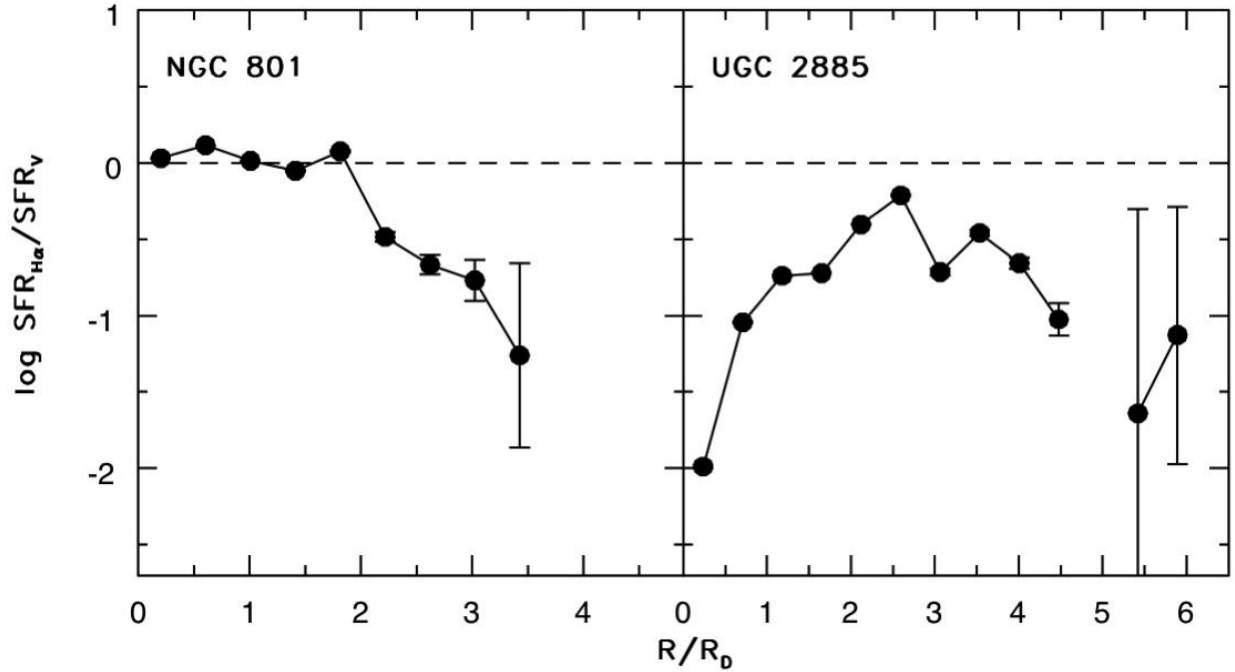


Fig. 12.— SFR derived from $H\alpha$ divided by the lifetime-averaged SFR derived from the stellar mass, determined from the V -band surface brightness corrected to face-on. The horizontal dashed line at 0 marks the value for equal SFRs. The current star formation activity, $\text{SFR}_{H\alpha}$, is everywhere much lower than that averaged over the lifetime of the galaxies, SFR_V . For UGC 2885, there is no $H\alpha$ emission in the third to last azimuthally-averaged annulus (60 kpc radius); hence, there is a discontinuity in the $\text{SFR}_{H\alpha}$ profile.

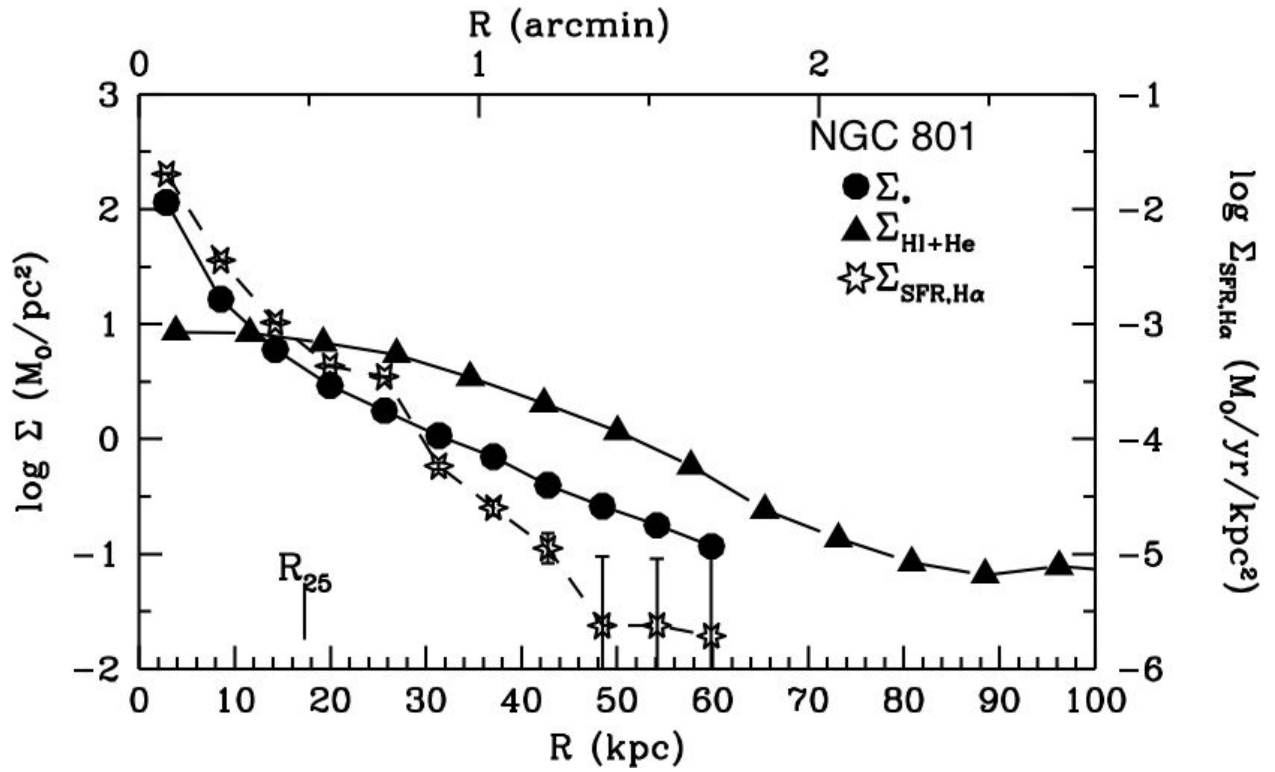


Fig. 13.— Stellar mass surface density Σ_* , HI+He surface density $\Sigma_{\text{HI+He}}$, and SFR density $\Sigma_{\text{SFR,H}\alpha}$ plotted as a function of radius for NGC 801. The gas and stellar mass surface densities have been corrected to face-on. The logarithmic interval is the same for all three quantities, but the SFR zero point is different.

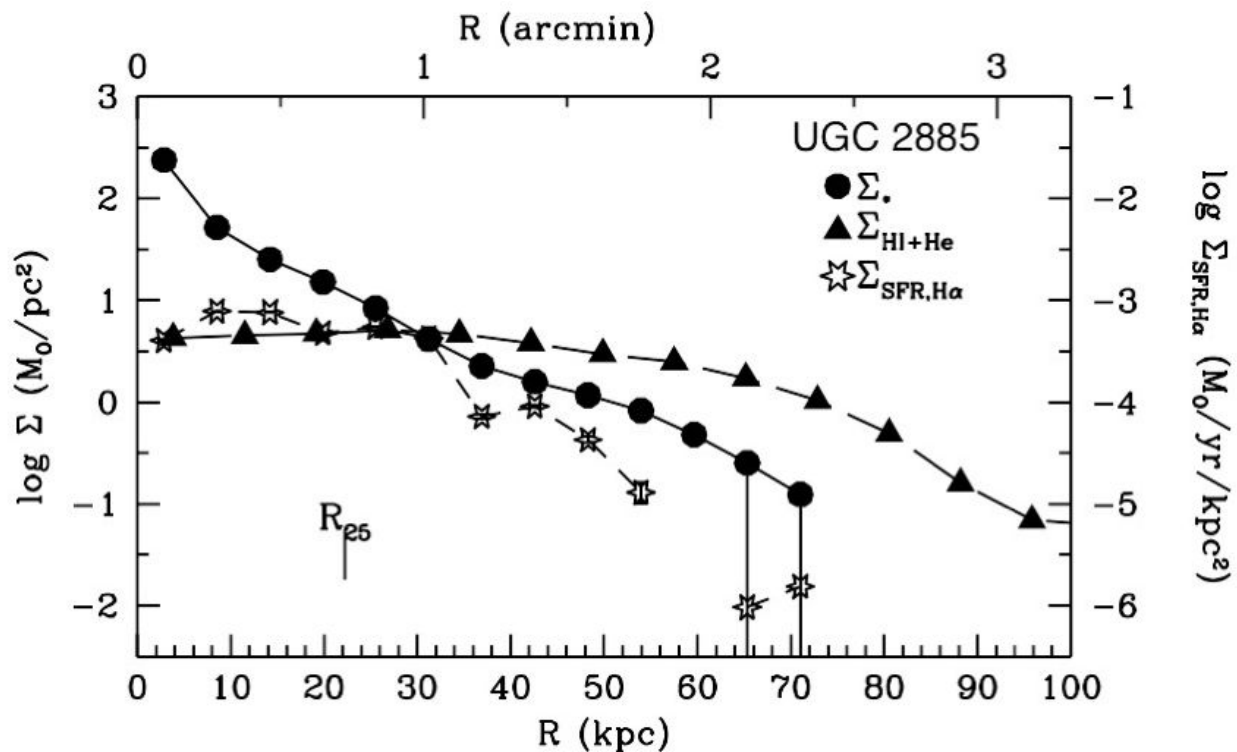


Fig. 14.— Stellar mass surface density Σ_* , HI+He surface density $\Sigma_{\text{HI+He}}$, and SFR density $\Sigma_{\text{SFR,H}\alpha}$ plotted as a function of radius for UGC 2885. The gas and stellar mass surface densities have been corrected to face-on. The logarithmic interval is the same for all three quantities, but the SFR zero point is different. There is no H α emission in the third to last azimuthally-averaged annulus (60 kpc radius); hence, there is a discontinuity in the SFR $_{\text{H}\alpha}$ profile.

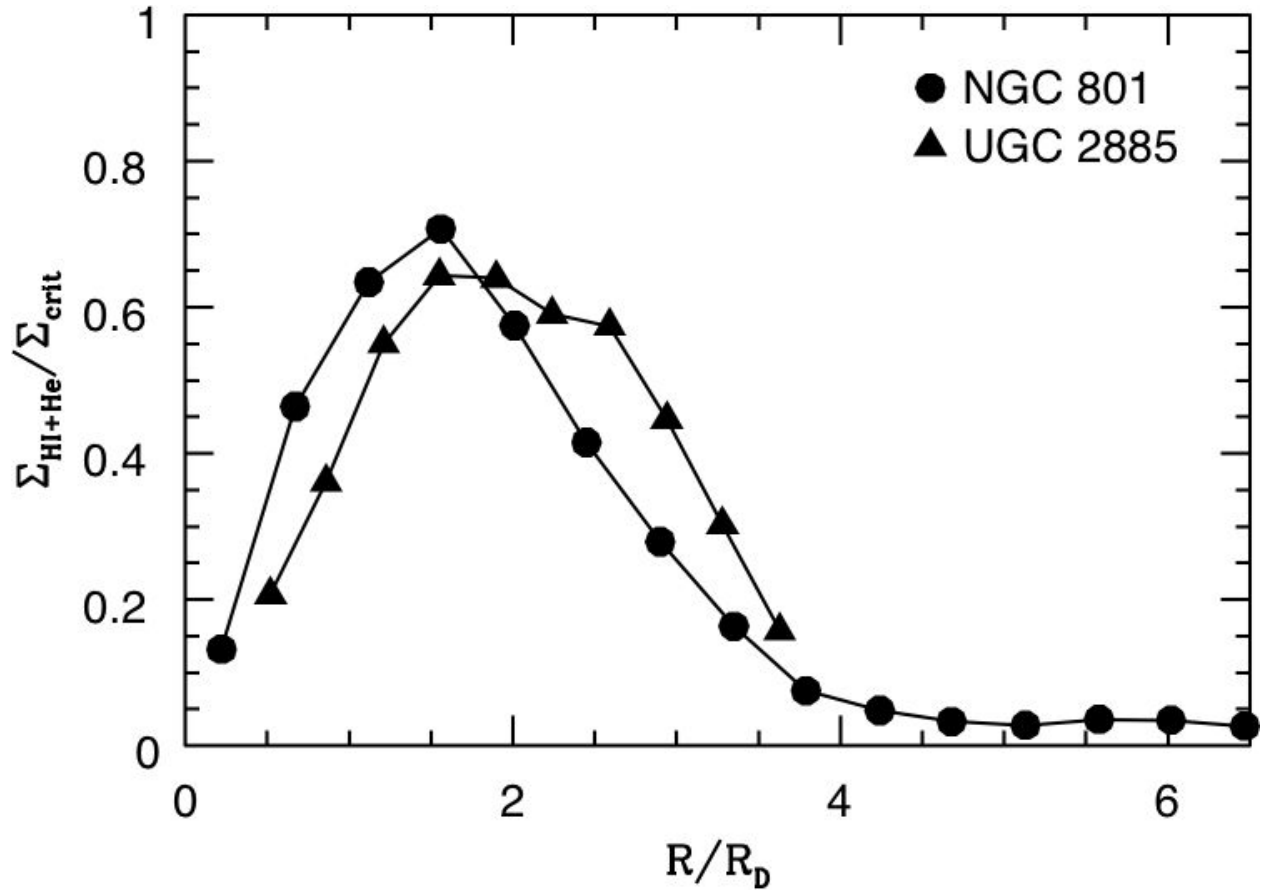


Fig. 15.— Ratio of HI+He gas surface density to critical gas density predicted by the gravitational instability model of Toomre (1964) versus radius in units of disk scale length.

Table 1. Galaxy Characteristics

Parameter	NGC 801	UGC 2885
D (Mpc) ^a	79.4	79.1
Center (h m s, deg arcmin arcsec; J2000) ^b	2:03:45.4 38:15:32	3:53:02.5 35:35:22
PA (deg) ^b	–28	47.5
b/a ^b	0.24	0.33
Incl (deg) ^b	82	74
$E(B-V)_f$ ^c	0.042	0.176
$E(B-V)_i^{HII}$ ^c	0.18	0.15
M_V ^d	-21.99 ± 0.005	-22.71 ± 0.007
$\log M_{HI}$ (M_\odot)	10.48	10.62
$R_{1/2}$ (kpc) ^e	15.4	22.2
R_{25} (kpc) ^f	17.3	22.2
R_D (kpc) ^g	14.14 ± 0.52	12.05 ± 0.41
μ_V^0 (mag of 1 arcsec ²) ^h	23.09 ± 0.14	21.26 ± 0.15
$\log L_{H\alpha}$ (ergs s ⁻¹) ⁱ	41.6	41.5
$\log \text{SFR}_{H\alpha}$ ($M_\odot \text{yr}^{-1}$) ^j	0.50	0.41

^aDetermined from V_{GSR} , taken from NED and a Hubble constant of 75 km s⁻¹ Mpc⁻¹.

^bDetermined from the V -band image. The inclination assumes an intrinsic b/a of 0.2.

^cForeground reddening $E(B-V)_f$ from Schlafly & Finkbeiner (2011). Internal reddening $E(B-V)_i^{HII}$ from Prescott et al. (2007) for star-forming regions. For the field star $E(B-V)_i^*$, we multiply $E(B-V)_i^{HII}$ by 0.44 (Calzetti 1997). The value of $E(B-V)_i^{HII}$ given here is evaluated at the V -band half-light radius $R_{1/2}$, determined before the reddening corrections were applied.

^dCorrected for foreground extinction using $A_{V,f}/E(B-V)_f=3.1$ (Cardelli et al. 1989) and the internal extinction determined at the half light radius using $A_{V,i}/E(B-V)_i^*=4.05$ (Calzetti et al. 1994, 2000).

^eHalf-light radius of galaxy in the V -band not corrected for extinction.

^fRadius of galaxy at B -band isophote of 25 mag of 1 arcsec² before the extinction correction was applied.

^gDisk scale length determined from the fit to the outer disk V -band surface photometry, corrected for extinction. R_D for NGC 801 is for the outer component of the surface brightness profile.

^hCentral surface brightness of the stellar disk from the fit to the outer disk V -band surface photometry.

ⁱIntegrated $H\alpha$ luminosity, corrected for extinction using the value appropriate to $R_{1/2}$. This value has also been corrected for [NII] emission in the filter bandpass (see §3.3.1).

^jIntegrated SFR determined from $L_{H\alpha}$ using the formula of Kennicutt (1998) (see §3.3.3).